Research Square

Preprints are preliminary reports that have not undergone peer review.
They should not be considered conclusive, used to inform clinical practice,
or referenced by the media as validated information.

Heterogeneous van der Waals integration of single-crystalline photonic nanomembranes

Sang-Hoon Bae

sbae22@wustl.edu

Washington University in St. Louis https://orcid.org/0000-0002-1518-7635

Yuan Meng

Washington University in St Louis https://orcid.org/0000-0002-5409-5610

Wenbo Mao

Washington University in St Louis https://orcid.org/0000-0002-7406-0992

Zhihao Xu

Washington University in St. Louis

Di Jia

Washington University in St Louis

Mengxin Lin

Swiss Federal Technology Institute of Lausanne

Jisung Seo

University of Illinois Urbana-Champaign

Bora Kim

University of Illinois Urbana-Champaign

Xinyuan Zhang

Massachusetts Institute of Technology https://orcid.org/0000-0002-5135-2204

Eugene Park

Massachusetts Institute of Technology https://orcid.org/0000-0001-6573-9162

Seokje Lee

Massachusetts Institute of Technology

Jekyung Kim

Massachusetts Institute of Technology https://orcid.org/0000-0002-8250-5736

Sangmoon Han

Washington University in St. Louis https://orcid.org/0000-0001-7924-2050

Ji-Yun Moon

Washington University in St. Louis

Weijie Xu

Washington University in St Louis

Qian Zhang

Washington University in St Louis

Xiaoqing He
Washington University in St. Louis

Mingfeng Chen
Washington University https://orcid.org/0000-0001-8408-0359

Sang Hyun Nam
Hanyang University

Jianqi Hu
Swiss Federal Institute of Technology Lausanne (EPFL)

Justin Kim
Washington University in Saint Louis

Sejin Lee
Washington University in St. Louis

Sanggeun Bae
Washington University in St. Louis https://orcid.org/0009-0005-1726-8868

Soo Ho Choi
University of Illinois Urbana-Champaign

Tae Hyung Kim
Washington University in St. Louis

Yunseok Choi
Washington University in St. Louis

Seung-Il Kim
Washington University in St. Louis

Kyubeen Kim
Washington University in St. Louis

Minho Jin
Washington University in St. Louis

Chen Jiang
Washington University in St. Louis

Yiheng Zhang
Washington University in St. Louis

Young-Hoon Kim
Hanyang University https://orcid.org/0000-0003-1810-6885

Jae-Hyun Lee
Ajou University https://orcid.org/0000-0001-5117-8923

Hobeom Kim
Gwangju Institute of Science and Technology https://orcid.org/0000-0002-5296-8975

Sheng Ran
Washington U in St. Louis https://orcid.org/0000-0003-1557-267X

Xi Wang
Washington University https://orcid.org/0000-0002-0641-0882
Cheng-Wei Qiu
National University of Singapore https://orcid.org/0000-0002-6605-500X
Frances Ross
Massachusetts Institute of Technology https://orcid.org/0000-0003-0838-9770
Jeehwan Kim
Massachusetts Institute of Technology https://orcid.org/0000-0002-1547-0967
Minjoo Lee
University of Illinois Urbana-Champaign https://orcid.org/0000-0002-3151-3808
Hyunseok Kim
University of Illinois Urbana-Champaign https://orcid.org/0000-0003-3091-8413
Tobias Kippenberg
Swiss Federal Institute of Technology Lausanne (EPFL) https://orcid.org/0000-0002-3408-886X
Lan Yang
Washington University in St. Louis

Physical Sciences - Article

Keywords:

Posted Date: December 18th, 2025

DOI: https://doi.org/10.21203/rs.3.rs-8301417/v1

License: This work is licensed under a Creative Commons Attribution 4.0 International License.
Read Full License

Additional Declarations: There is **NO** Competing Interest.

Version of Record: A version of this preprint was published at Nature on September 16th, 2026. See the published version at https://doi.org/10.1038/s41586-026-11000-w.

Heterogeneous van der Waals integration of single-crystalline photonic nanomembranes

Yuan Meng[1†], Wenbo Mao[2†], Zhihao Xu[3†], Di Jia[2†], Mengxin Lin[4,5], Jisung Seo[6,7], Bora Kim[7,8], Xinyuan Zhang[9], Eugene Park[9], Seokje Lee[10,11], Jekyung Kim[10,11], Sangmoon Han[1], Ji-Yun Moon[1], Weijie Xu[2], Qian Zhang[2], Xiaoqing He[3], Mingfeng Chen[12], Sang Hyun Nam[13], Jianqi Hu[4,5], Justin S. Kim[3], Sejin Lee[3], Sanggeun Bae[3], Soo Ho Choi[7,8], Tae Hyung Kim[1,13], Yunseok Choi[1], Seung-Il Kim[1], Kyubeen Kim[1], Minho Jin[1], Chen Jiang[1], Yiheng Zhang[2], Young-Hoon Kim[13], Jae-Hyun Lee[14], Hobeom Kim[15], Sheng Ran[12], Xi Wang[12], Cheng-Wei Qiu[16], Frances M. Ross[9], Jeehwan Kim[9,10,11], Minjoo Larry Lee[6,7,8], Hyunseok Kim[6,7,8,17], Tobias J. Kippenberg[4,5], Lan Yang[2,3]*, and Sang-Hoon Bae[1,3,12]*

[1]Department of Mechanical Engineering and Materials Science, Washington University in St. Louis, St. Louis, MO, USA.
[2]Department of Electrical and Systems Engineering, Washington University in St Louis, St. Louis, MO USA.
[3]Institute of Materials Science and Engineering, Washington University in St Louis, St. Louis, MO, USA.
[4]Institute of Physics, Swiss Federal Institute of Technology Lausanne (EPFL), Lausanne, Switzerland.
[5]Institute of Electrical and Micro Engineering (IEM), Swiss Federal Institute of Technology (EPFL), Lausanne, Switzerland.
[6]Department of Materials Science and Engineering, University of Illinois Urbana-Champaign, Urbana, IL, USA.
[7]Holonyak Micro and Nanotechnology Laboratory, University of Illinois Urbana-Champaign, Urbana, IL, USA.
[8]Department of Electrical and Computer Engineering, University of Illinois Urbana-Champaign, Urbana, IL, USA.
[9]Department of Materials Science and Engineering, Massachusetts Institute of Technology, Cambridge, MA, USA.
[10]Department of Mechanical Engineering, Massachusetts Institute of Technology, Cambridge, MA, USA.
[11]Research Laboratory of Electronics, Massachusetts Institute of Technology, Cambridge, MA, USA.
[12]Department of Physics, Washington University in St Louis, St Louis, MO, USA.
[13]Department of Energy Engineering, Hanyang University, Seoul, Republic of Korea.
[14]Department of Electrical and Computer Engineering, Sungkyunkwan University, Suwon, Republic of Korea.
[15]Department of Materials Science & Engineering, Gwangju Institute of Science and Technology, Gwangju, Republic of Korea.
[16]Department of Electrical and Computer Engineering, National University of Singapore, Singapore, Singapore.
[17]Materials Research Laboratory, University of Illinois Urbana-Champaign, Urbana, IL, USA.
† Equal contribution.
Correspondence: sbae22@wustl.edu; lyang25@wustl.edu;

Abstract

Albeit the speed and energy advantages offered by silicon (Si) and silicon nitride (SiN) photonics[1], a single material platform, with varying intrinsic limitations, can hardly meet the ever-diversifying requirements posed for photonic integrated circuits (PICs)[2,3]. The heterogeneous integration of functional materials to established photonic platforms has thus gained tremendous momentum[4], underpinning various high-performance optoelectronic applications[5]. However, stringent lattice-matching constraints severely hinder the heteroepitaxial material quality grown on dissimilar optical substrates[6]. Here we obviate this hurdle by exploiting freestanding single-crystalline nanomembranes enabled by advanced epitaxy and layer lift-off techniques[7-10]. We present a versatile framework leveraging photonic van der Waals (vdW) integration[11] to infuse desired functionalities to Si and SiN photonics. By transferring single-crystalline thin-film barium titanate (BTO) to Si chips, we experimentally demonstrate ultraefficient electro-optical (EO) modulation, featuring giant Pockels coefficient r_{42} over 1290 pm/V and a 3 dB EO bandwidth over 23 GHz, enabled by well-defined BTO crystallographic quality and orientations. Ultracompact non-reciprocal magneto-optical (MO) isolators are further realized, via vdW-integrating cobalt ferrite (CFO) nanomembranes to Si microrings, manifesting an ultrahigh Faraday rotation coefficient θ_F exceeding 33,800 °/cm. To embody the salient capabilities of coalescing functional materials with disparate crystal structures to arbitrary photonic templates, we laterally stitch gallium arsenide[12,13] and gallium nitride single-crystals[14-16] atop SiN photonics to realize expansive photodetection from ultraviolet to near infrared wavelengths[17]. Multifunctional ring-resonators for simultaneous EO and MO modulations are also demonstrated by constructing vertical CFO/BTO heterostructures, ushering a vast playground to prototype record-setting heterogeneous integrated applications and study diverse physical coupling phenomena[18-20].

1. Main

Photonic integration has enabled a vast variety of technologies by offering unparalleled capabilities in speed, bandwidth, and power efficiency[3]. Despite the fruitful successes on Si and SiN photonics from optical communications to sensing and imaging[1,21], they manifest varying intrinsic material limitations[5] such as lacking EO modulation, MO isolation, lasing, and wide-spectrum photodetection capabilities. Heterogeneous photonic integration has thus drawn tremendous interest from both academia and industry[2,3,22,23], by coalescing the unique advantages from different material platforms towards multifunctional fully integrated photonic circuits and systems[4,24].

However, conventional approaches relying on heteroepitaxy encounter rigid lattice matching and process compatibility constraints, greatly restricting the available material combinations for heterogeneous integration. When significant lattice mismatch exists between the desired functional material and optical substrate, which is ubiquitous in photonic layouts, substantial defects will be generated[25]. The resultant epilayer will be severely deteriorated in intrinsic material attributes, greatly compromising device performance[6]. Various endeavors have been made to pursue high-quality, ideally single-crystalline, functional optical layers on lattice-mismatched low-index substrates such as silicon dioxide[26]. Successful explorations include crystal ion slicing and bonding techniques[27], such as the recent achievements in integrating EO crystals lithium niobate (LN)[28-32] and lithium tantalate (LT)[33,34] on insulator. Nevertheless, they still confront limitations on inevitable ion implantation crystal damage[27] and sophisticated costly procedures. Therefore, a versatile and universal platform to heterogeneously integrate multiple functional single-crystalline thin films on an arbitrary optical substrate is still an open challenge.

Van der Waals (vdW) integration[11], a physical assembly strategy stemming from two-dimensional (2D) materials community leveraging exfoliated freestanding films[6,35], offers a promising alternative to address the abovementioned challenges with emerging opportunities. The advent of epitaxy and layer lift-off techniques[12,15,18,36] now facilitates a panoply of freestanding functional three-dimensional (3D) nanomembranes for boundless heterogeneous integration[7,8,10,11,17]. Desired functional layers can be prepared with single-crystallinity at their most suitable lattice-matched parent substrates, and get delaminated into freestanding nanomembranes[9,18,36], preserving optimal intrinsic material quality. An extensive library of 3D vdW building blocks[11] can thus be readily transferred to arbitrary templates[6] to enable record-breaking device performance and prototype novel integrated applications[7,9,10,37]. Circumventing the lattice-matching constraints bounded by heteroepitaxy, vdW integration can harvest the most favorable functionalities from multiple dissimilar material platforms with low-cost and unprecedented freedom[4,6] for advancing heterogeneous integrated photonics.

Here we present a comprehensive photonic vdW integration framework, based on diverse freestanding single-crystalline 3D nanomembranes[11] with optimal optical functionalities but distinct crystal structures to construct prodigious high-performance hetero-integrated photonics. Cardinal optical applications are exemplified, encompassing EO modulation[29-32], MO isolation[38-

[40] and extensive on-chip photodetection[22,41] (Fig. 1a). Exploiting epitaxial lift-off[9,36,37] and 2D materials-assisted layer transfer (2DLT) techniques[7,10,12,17,18], various functional 3D nanomembranes are synthesized, including EO material barium titanate ($BaTiO_3$, BTO)[24,42-47], MO material cobalt ferrite ($CoFe_2O_4$, CFO)[7,48-50] and yttrium iron garnet ($Y_3Fe_5O_{12}$, YIG)[38,51], and group III-V semiconductors gallium arsenide (GaAs)[13,16] and gallium nitride (GaN)[14] with precisely-controlled film thickness and well-preserved bulk-like material properties.

By selecting required 3D functional Lego bricks[7,11], unbridled heterogeneous integration layouts are constructed in a way resembling building various 2D vdW heterostructures[7,10,18,35] up to wafer-scale[14,16,17], imparting arbitrary desired functionalities to mature photonic platforms such as Si, SiN, and beyond. Via vdW integrating BTO nanomembranes to Si photonics with engineered crystal orientations, we demonstrate record-setting high-efficiency EO modulators with ultralow half-wave voltage-length product $V_\pi L$ of 0.29 V·cm, corresponding to a giant in-plane effective Pockels coefficient r_{eff} as 950 pm/V and a Pockels tensor component $r_{42} > 1290$ pm/V, which is about 40 times higher than LN[27]. Likewise, highly efficient MO modulation is also realized by transferring single-crystal CFO nanomembranes to Si microring resonators. The extracted Faraday rotation coefficient θ_F is found to be 33,800 °/cm, around 100 times higher than YIG[52] and 10 times higher than Ce: YIG[38-40,53,54].

To further exemplify design flexibility, we laterally integrate GaAs and GaN nanomembranes[14,16] atop a single SiN chip, delivering an expanded Schottky photodetection range from ultraviolet (UV) to near infrared (NIR). Moreover, we vertically stack single-crystalline CFO/BTO artificial 3D heterostructures onto Si micro-resonators to enable multifunctionality: efficient EO modulation and MO isolation realized in a single-device. Taken together, this work establishes a scalable and viable platform for heterogeneous photonic integration, enabling next-generation photonic applications that combine disparate single-crystalline materials into single photonic architecture[11]. An exciting playground also unfolds by further expanding the vdW heterostructures concept[6,35], from 2D to 3D and beyond, to handily study variegated nanophotonic physical couplings from classic to quantum and topological realms[18-20].

2. Functional single-crystalline nanomembranes for photonic vdW integration

Epitaxy of 3D crystals[25] typically requires a single-crystalline substrate with matched lattice parameters for obtaining high-quality epilayers[36,55], since the adatoms can replicate the atomic registry from the substrate with strong chemical bonds. However, the optical refractive index and material functionality of the suitable heteroepitaxy combos, such as BTO/STO (strontium titanate) and YIG/GGG (gadolinium gallium garnet), are usually very approaching[39], precluding most integrated applications that need refractive index contrast for optical confinement. Delaminating single-crystalline 3D layers from lattice-matched grown substrates thus circumvents this canonical challenge, enabling boundless heterogeneous integration[11].

We employed two schemes to prepare high-quality freestanding 3D optical nanomembranes for photonic vdW integration (Supplementary Fig. S6). One is 2DLT enabled by remote epitaxy[12] (Fig.

1b), an emerging technology utilizing 2D-monolayers-coated epitaxial templates to create single-crystalline freestanding thin films[7,10,16-18,25]. The 2D materials, such as graphene and boron nitride, act as an ultrathin interlayer that allows the penetration of atomic potential from the substrate to enable remote adatoms interactions[15], permitting the epitaxy of single-crystalline films[56]. As the semitransparent 2D layers prohibit the formation of covalent bonds between the epitaxial layer and substrate[12], the epilayer can be mechanically exfoliated from substrate with atomically smooth interfaces[9] (Fig. 1c) in a fast[57], cost-saving[18], wafer-scale, and high-throughput manner[14,16].

The other approach is epitaxial lift-off (ELO)[8,36], also called chemical lift-off, where the grown film is released by selectively etching the judiciously chosen sacrificial layers[58,59] (Fig. 1d). A layered epitaxial stack is first synthesized[8], followed by coating a handling layer, such as polymer or metal, and a wet transfer process[11] (Fig. 1e). These delaminated functional 3D thin-films (Supplementary Notes 1, 2) can be heterogeneously assembled like 2D materials, via lateral stitching or vertical stacking with optionally engineered interlayer rotation angles to unlock moiré superlattices[19,20] and artificial 3D heterostructures (Fig. 1f). For instance, we construct heteroepitaxy-inaccessible GaAs/BTO/GaN/STO heterostructures on SiO_2 substrate, where all stacked layers are single-crystalline (Supplementary Note 3, Fig. S10) verified by high-resolution scanning transmission electron microscopy (HR-STEM).

For EO material BTO, a water-dissolvable thin sacrificial layer $Sr_3Al_2O_6$ (SAO)[60-62] is epitaxially grown on (100) single-crystalline STO substrate in high-vacuum condition (Methods), followed by BTO layer epitaxy with alleviated temperature[37,62]. Owing to the matched lattices of the BTO/SAO/STO stack, high-quality tetragonal BTO films are obtained with minimal stress[37] (Supplementary Note 2), and controlled crystallographic orientation through engineered annealing and cooling procedures (Supplementary Note 4, Fig. S11) for strong in-plane Pockels response. For MO materials CFO and YIG, a magnesium oxide (MgO) thin layer is first grown atop (100) single-crystalline MgO substrates. Optimized domain-matching epitaxy[63] is applied for CFO[64] or YIG[65] epilayers (Methods). Weak acidic solutions, such as acetic acid or ammonium sulfate, have negligible reactions with CFO and YIG to facilitate ELO. Remote epitaxy[12] is also explored for YIG[7,51], GaN[14,15], and GaAs[10,16] with graphene- or BN-coated substrates (Methods, Supplementary Note 5).

These epilayers are then exfoliated from their parent substrates into freestanding 3D vdW building blocks[11] via ELO or 2DLT depending on growth methods (Fig. 1g). Excellent single-crystalline film quality is confirmed by the asymmetric ϕ-scanning X-ray diffraction (XRD) (Fig. 1h, Supplementary Note 2), and electron backscatter diffraction (EBSD) (Fig. 1i) measurements.

3. EO modulation by freestanding BTO single-crystals

Armed with plenteous freestanding 3D nanomembranes, heterogeneous photonic integration is empowered via vdW assembly[6]. Among various integrated applications, EO process is a pivotal nonlinear optical phenomenon enabling high-speed modulation[29,30,33], microwave photonic

processing[28,32,34], and beyond. Compared with other physical mechanisms such as free-carrier dispersion, thermo-optics, and acousto-optics, EO response permits the fastest control of photonics via high-speed electronics[27]. LN and BTO are two paradigms with linear EO effect, namely Pockels effect[66], where the refractive index change Δn of the EO material is proportional to the applied static or radio-frequency (RF) electric field E_{RF}:

$$\Delta n = -\frac{1}{2} n_{(0)}^3 r_{\mathrm{eff}} E_{\mathrm{RF}}, \quad (1)$$

where $n_{(0)}$ is the unperturbed optical refractive index[42], r_{eff} denotes effective Pockels coefficient (Methods), which highly depends on the crystallographic orientation of the EO material, and the designed vectorial distributions of $\mathbf{E}_{\mathrm{RF}}$ and optical polarization $\mathbf{E}_{\mathrm{opt}}$ (Supplementary Notes 6, 7). However, ion-sliced single-crystalline LN has limited $r_{\mathrm{eff}} \approx r_{33} \approx$30 pm/V[27,29,30]. The pursuit of highly efficient Pockels materials, towards ultimate PIC device miniaturization and energy consumption reduction, has drawn enormous attention to BTO, a perovskite-structured oxide possessing among the highest Pockels tensor components $r_{42} = r_{51}$ around 1300~1600 pm/V measured in bulk crystals[44,47,66].

Nevertheless, currently reported in-plane Pockels coefficient values of BTO films drastically varies, from several tens[67,68] to a few hundred picometre per Volt[24,42,45,46]. This is primarily attributed to compromised polycrystal quality and not rigorously controlled crystallographic orientations of the grown BTO films (Supplementary Note 7). Promising BTO heteroepitaxy on Si with attentively-optimized STO buffer layer via molecular beam epitaxy (MBE)[44-46] has been reported for integrated EO devices, followed by layer bonding and complex substrate grinding procedures[24,43]. Such method yields improved BTO crystallinity with[43] $r_{42} \approx$ 923 pm/V, yet still faltering behind the intrinsic giant Pockels coefficient found in bulk crystals[66], due to the fundamental epitaxial limits of growing lattice-mismatched STO buffer on Si. Mechanical spalling[36] from BTO bulk crystal is still in its infancy as well[47], with piles of pending works on resultant film morphology and roughness improvement[47] before reliable BTO integration.

Here we repot a viable alternative for BTO heterogeneous photonic integration[11], using freestanding single-crystalline BTO nanomembranes[37] with precisely controlled thickness and sizes from hundreds of square millimeters to 1-inch wafer scale (Supplementary Note 1). Atomic force microscopy (AFM) confirms the low root mean square (RMS) roughness below 0.2 nm for our pulsed laser deposition (PLD)-grown BTO film surface before layer lift-off (Fig. 2a). Despite some large effective Pockels coefficients $r_{\mathrm{eff}}^{\perp}$ measured perpendicular to BTO film[24,67], integrated photonic applications require dominant in-plane Pockels response[42,45], corresponding to a-axis-domain BTO (crystallographic BTO c-axis parallel to film plane, Supplementary Notes 7). We verified well-defined crystallographic orientation of the delaminated a-axis BTO single-crystal resting on polydimethylsiloxane (PDMS) by 2θ-ω-scanning XRD (Fig. 2b), with ultranarrow BTO (200) Bragg peak (Supplementary Note 2). Detailed reciprocal space mapping (RSM) reveal three possible BTO crystallographic orientations (Fig. 2c), where BTO a-axis-domains are proven predominant than c-axis-domains (with BTO c-axis perpendicular to film, Supplementary Note 8),

achieved via synergistically engineered film growth processes (Methods, Supplementary Note 4). Signature butterfly-shaped BTO ferroelectric hysteresis loop is also observed (Supplementary Fig. S9e). Given that multiple ferroelectric domain orientations can arise from the epitaxial strain relaxation in thermodynamic film growth and cooling processes[43,46], post-transfer poling[42] and judicious alignment of BTO crystal axis relative to the applied RF electric field and optical polarization directions are crucial for EO device operation[66] (Methods). For our a-axis-domain BTO, the effective Pockels coefficient r_{eff} maximizes when the film is sufficiently poled and deliberately rotated[42,43] by an angle $\theta = 45°$ (Supplementary Note 7).

$$r_{\mathrm{eff}}^{\max} = \sqrt{2}(2r_{42} + r_{33} + r_{13})/4 \quad (2)$$

Therefore, during BTO vdW integration, BTO nanomembranes are rotated by $\theta \approx 45°$ between the film (100) edge and the waveguide direction (Supplementary Note 1). Uniform and robust nanomembrane bonding to prefabricated Si photonic chips (Supplementary Note 9) is achieved with atomically clean and electronically sharp interfaces[11] (Supplementary Fig. S21). We transferred a 120 nm-thick BTO to a set of Si microring resonators via polypropylene carbonate (PPC) handler (Methods)[7,37]. Scanning electron microscopy (SEM) shows smooth surface morphology and solid film bonding to substrate (Fig. 2d). By comparing the quality factors (Q) of the micro-resonator before and after BTO transfer (Fig. 2e), the total optical loss increment is estimated to be 2.5 dB/cm, ensuring low-loss heterogeneous photonic integrations.

A 100-nm thick a-axis-domain BTO nanomembrane is vdW integrated onto silicon-on-insulator (SOI) photonic chips with Mach-Zehnder structures (Fig. 2f). A reduced waveguide dimension is selected in order to enhance the optical modal overlap between the Si waveguide and the EO layer above it (Supplementary Note 10). The simulated RF electric field $|\mathbf{E}_{\mathrm{RF}}|$ and optical field $|\mathbf{E}_{\mathrm{opt}}|$ distributions along the BTO Mach-Zehnder modulator (MZM) waveguide cross-section (Fig. 2g) evince good optical confinements (device structure detailed in Supplementary Fig. S17a). An ultralow half-wave voltage-length product $V_\pi L$~0.29 V·cm is experimentally measured at 1 KHz voltage frequency at 1550 nm wavelength (Fig. 2h). Giant effective Pockels coefficient is extracted from the experimental data as r_{eff}~950 pm/V (Methods), corresponding to an estimated BTO Pockels tensor component $r_{42} > 1290$ pm/V (Supplementary Notes 6 and 11), which is about 40 times higher than LN[27,28] or LT[33,34], and ~10 times higher than lead zirconate titanate (PZT)[66] (Supplementary Notes 12).

Albeit strong Pockels response, the BTO MZMs discussed above in Fig. 2h only carry an EO 3dB bandwidth of a few gigahertz, hindering high-speed EO applications[24]. Further enhancing the EO bandwidth of the BTO MZMs necessitating device structure redesign with travelling-wave electrodes and revisiting the trade-offs between half-wave voltage V_π and operation bandwidth(Supplementary Note 10). Supplementary Fig. S17b illustrates the modified MZM design based on vdW-integrated BTO/Si hybrid heterostructures. A 45 nm-thick a-axis-domain BTO is selected, with a 250 nm-thick SiO_2 cladding added between the BTO layer and gold electrodes (Fig. 2i), to catch the target 50 Ω characteristic impedance Z_0 and balance the group

velocities[27,29,30,33] between microwave n_g^{RF} and optics n_g^{Opt} (Supplementary Note 10). High-resolution scanning transmission electron microscopy (HR-STEM) confirms excellent BTO nanomembrane bonding and well-defined crystallographic orientation (Fig. 2j, Supplementary Note 13). We experimentally verified high-speed EO modulation with a 3 dB bandwidth over 23 GHz (Fig. 2k) and a $V_\pi L\sim$ 1.4 V·cm measured with a 2 MHz triangular voltage sweep (Supplementary Fig. S24). We note that this EO bandwidth, though already surpassing previous reported BTO-MZMs[24,67] and comparable to BTO microring-based EO modulators[43,45], is currently limited by nonideal device fabrication (Supplementary Note 14). The extracted r_{eff} for this high-speed BTO-MZM is around 880 pm/V, corresponding to r_{42}~1190 pm/V (Supplementary Note 6), consistent with further electromagnetic simulations (Supplementary Notes 11). This promises ultraefficient high-speed integrated EO applications[24,28] (Supplementary Note 12) and multifunctional photonic devices vdW-integrated with multiple functional materials discussed later.

4. Integrated photodetection by freestanding III-V semiconductors

Besides EO modulation, group III-V semiconductors featuring outstanding optoelectronic properties with direct and widely-engineerable bandgaps[4,5], also underpin indispensable PIC components such as optical amplifiers[2], lasers[3,23], and photodetectors[22,41]. Distinctive from growth-based approaches, here we demonstrate waveguide-coupled expansive photodetectors by vdW integrating freestanding single-crystalline ELO GaAs and 2DLT GaN films to prefabricated SiN photonics (Supplementary Note 9). This scheme endows both single-crystalline III-V quality and the versatility to interface with additional functional layers for multitudinous devices- to systems-level upscaling[10,18]

High-quality GaAs films are grown by MBE[13] with designed positive-intrinsic-negative (p-i-n) doping layers (Methods, Supplementary Fig. S3a), followed by ELO layer delamination (Supplementary Notes 1, 15). STEM images confirm the highly uniform and seamless GaAs film bonding to the SiN substrate (Fig. 3a). HR-TEM verifies the single-crystalline quality of the GaAs nanomembranes with clear lattice fringes (Fig. 3b, Supplementary Note 16). Figure 3c shows the fabricated device by vdW-integrating GaAs to SiN photonic chip with predefined gold bottom contacts (BC) and smooth GaAs film surface (Fig. 3d). Despite a suspended air gap height $h \approx 30$ nm between the GaAs layer and SiN waveguide due to BC thickness (Methods), effective light-absorption still takes place as illustrated by electromagnetic simulations along the longitudinal waveguide cross-section (Fig. 3e). Experimental current-bias volage (I-V) curves are measured under different optical power fed by the SiN waveguide at 780 nm wavelength (Fig. 3f, Supplementary Note 17), corresponding to a competitive photoresponsivity of 0.23 A/W (Fig. 3g, Supplementary Note 18).

Proof-of-concept on-chip photodetection is also explored for remote epitaxial freestanding GaN single-crystals[14,56]. Atomically clean and electronically sharp interfaces of the exfoliated nanomembranes are entitled thanks to 2DLT[10,12,17] (Fig. 3h). It facilitates single-crystalline GaN quality[16] hetero-integrated on device (Fig. 3i), rapid layer release[15] without time-consuming

etching process tied to ELO, and reduced manufacture cost by recycling the costly epitaxial substrates[14].

Empowered by the high design freedom of photonic vdW integration[11], expanded wide-spectrum photodetection is enabled by heterogeneous vdW integration of different III-V nanomembranes with different bandgaps, as a straightforward yet proven highly efficacious scheme[17]. We laterally stitch ELO GaAs and 2DLT GaN films atop a SiN chip (Fig. 3j) with robust film bonding and patterning (Supplementary Note 15). Good film surface morphology (Fig. 3k), efficient light coupling from the SiN signal waveguide to III-V active layers (Fig. 3l), and feasible photodetection performance are confirmed (Fig. 3m). Photoresponsivity is measured over broad discrete wavelengths of 0.22 A/W at light wavelength $\lambda = 780$ nm, 0.16 A/W at $\lambda = 520$ nm, and 16.6 mA/W at $\lambda = 405$ nm (Fig. 3n) for this GaAs and GaN co-integrated chip (Supplementary Note 17). Despite proof-of-concept demonstration, this prototypical photodetector performance is comparable to prior literature based on waveguide-coupling structures (Supplementary Note 18) with upgraded design flexibility[10].

5. MO isolation by freestanding CFO single-crystals

Magneto-optics (MO) facilitates non-reciprocal photonic devices that break the time-reversal symmetry in light propagation[39], laying the foundation for essential applications including optical isolation, circulation, and energy-efficient in-memory photonic computing[38]. Exemplary MO materials, such as YIG and CFO[52], require exotic epitaxial substrates such as GGG and MgO incompatible with standard complementary metal-oxide-semiconductor (CMOS) process. Otherwise, deteriorated material performance is typically observed[36].

Utilizing vdW integration, we incorporate single-crystalline thin-film CFO[7] onto Si photonics, simultaneously unlocking high-performance on-chip non-reciprocal devices and efficient physical coupling with other functional nanomembranes[11,18] such as EO material. CFO is an inverse spinel ferromagnetic oxide with large MO gyrotropy, which is one of the highest among other insulating ferrites and garnets[49,50]. This furnishes highly efficient MO applications for CFO, with more stable magnetization and drastically stronger Faraday rotation coefficients θ_F than other ferrimagnetic materials like YIG[64].

Smooth film surface with RMS roughness below 0.2 nm (Fig. 4a) and evident ferromagnetic loop (Fig. 4b, Methods) of the PLD-grown CFO films are experimentally verified. These single-crystalline CFO nanomembranes are then delaminated from MgO substrate via ELO and PPC-assisted wet transfer (Methods, Supplementary Note 1), followed by lithographic patterning of the transferred CFO film atop prefabricated Si microring resonators (Fig. 4c, Supplementary Note 19). With an external neodymium permanent magnet placed proximity to the chip (Methods), non-reciprocal optical transmission is observed, with a splitting between clockwise (CW)- and counterclockwise (CCW)-propagating light with an extinction ratio (ER) over 18 dB (Fig. 4d). The transmission spectrum around $\lambda = 1550$ nm is shown as Fig. 4e, where no appreciable MO modulation is detected for TE mode. In addition, CFO is a hard magnetic ferrite with high

coercivity, where its material magnetism retains even after removing external magnetic field[48]. Magnet-free integrated optical isolator is thus realized (Supplementary Fig. S27) after magnetization of our CFO film (Supplementary Note 20), which is not accessible by soft magnetic garnets like YIG[39].

Our photonic vdW integration strategy[11] eliminates the previous challenging barriers of growing satisfactory CFO film atop of Si or SiN photonics that encumbers its widespread applications. Compared to the direct heteroepitaxial approaches utilizing buffer layers with compromised CFO quality[48-50,64], successful single-crystalline CFO hetero-integration is experimentally realized, with reduced optical loss due to mitigated optical scattering from film defects and surface roughness found in previous works[48] (Supplementary Note 19). A giant Faraday rotation coefficient of $\theta_F \sim 33{,}800°/\text{cm}$ is extracted from experimental data (Methods, Supplementary Note 21). Benefits from the single-crystallinity of the CFO nanomembranes, this θ_F is found around 100 times higher than YIG and 10 times higher than Ce: YIG[38-40,53,54] (Supplementary Note 23), which also outperforms prior literatures based on polycrystalline CFO grown on Si[48-50] (Supplementary Note 23).

Devoid of the thick remnant substrates[38,40] found in wafer bonding, vdW integration also enables coupling with other functional materials. Multifunctional photonic devices are further demonstrated, by vertical stacking freestanding MO and EO nanomembranes of CFO and BTO to build artificial 3D heterostructures on Si microring resonators with clean and sharp interfaces (Fig. 4f). An 80 nm-thick SiO_2 is deposited by plasma-enhanced chemical vapor deposition (PECVD), after completing BTO transfer to the prefabricated SOI microring chip (Methods), in order to protect the underlying layers from CFO wet etching (Supplementary Note 19). The resultant devices for simultaneous EO and MO modulations are shown as Fig. 5g. The simulated static electric field and magnetic field distributions for fundamental TE-mode (EO modulation) and TM-mode (MO isolation), respectively, are illustrated as Fig. 5h. Exemplary EO modulation (Fig. 5i) and resonant frequency tuning of this CFO/BTO hetero-integrated microring under different bias voltages (Fig. 5j) are experimentally observed. By adjusting the input laser polarization (Methods) and switching external magnetic field direction, MO modulation is confirmed with a nonreciprocal wavelength shift $\lambda_{MO} \approx 5$ pm and an ER over 13 dB (Fig. 5k). EO modulation and MO isolation under same optical mode are also feasible by judicious device design. Fully integrated devices can be envisaged as well by replacing external magnets to ring-shaped electromagnets atop CFO[38,40] (Supplementary Note 24), for expansive optoelectronic applications in data storage and spintronics[64].

6. Conclusions

Leveraging the versatile photonic vdW integration platform[11], diverse heterogeneous integration layouts, which are hardly accessible via conventional heteroepitaxy[36] (Supplementary Fig. S10), are now made feasible via the physical assembly of various single-crystalline 3D freestanding nanomembranes[7,10]. These 3D vdW building blocks[9], furnished with a vast collection of photonic

and optoelectronic functinalities[8], are readily transferred to arbitrary prefabricated optical templates to prototype record-setting devices or multifunctional hetero-integrated photonic applications with unrivalled design freedom[17]. We demonstrate vdW integrations from centimeter-sized 3D films for lab explorations, to large wafer-scale BTO transfer to promise scalable applications (Supplementary Note 25), verified with smooth surface, atomically sharp interface, and high robustness (Supplementary Fig. S31). After proper thermal treatments, the vdW gaps between stacked 3D layers are replaced by seamless solid bonding with validated high robustness (Supplementary Note 26), thanks to the rich dangling-bonds-decorated surfaces of these artificially delaminated 3D nanomembranes[36].

Heterogeneous vdW-integrations of functional optical layers with eminent material quality approaching bulk crystals are experimentally verified[12], surmounting the ubiquitous crystallinity deterioration issues found in direct-growth-based Si and SiN photonics hetero-integration[4,39,41]. This feature reveals particular advantage, when device performance exceedingly hinges on the crystallographic quality and orientation of the functional materials[52,66] such as BTO[42,43,45]. We demonstrate highly efficient BTO MZMs with ultralow $V_\pi L$ ≈0.29 V·cm, corresponding to a giant effective Pockels coefficient r_{eff} ≈ 950 pm/V (Fig. 5a), equivalent to r_{42} >1290 pm/V surpassing previous works[24,43,45-47,67] (Fig. 5b, Supplementary Note 12). High-speed EO modulation[24] is realized as well with a 3 dB EO bandwidth over 23 GHz. We also report efficacious MO non-reciprocal optical isolation by vdW-integration, showcasing a large Faraday rotation coefficient[48-50] θ_{F} ≈33,800°/cm with orders of magnitude higher than conventionally used garnets[38-40] (Fig. 5c, Supplementary Note 23).

Moreover, we further expand the vdW heterostructures concept to 3D nanomembranes. By lateral stitching GaAs[13,16,56] and GaN[14,15] single-crystals atop SiN photonics, extended photodetection from UV to NIR is experimentally measured at discrete wavelengths from different devices on same chip (Fig. 5d, Supplementary Note 18). By building vertical heterostructures of EO and MO nanomembranes of BTO and CFO on Si microring resonators, multifunctional hetero-integrated photonic devices are demonstrated for hybrid electromagnetic modulation. Our work establishes a general and viable framework for infusing desired functionalities to established Si and SiN photonics via vdW integration[11], with optimal single-crystallinity but utterly dissimilar crystal structures that are otherwise hardly attainable. An intriguing playground is also facilitated to construct exotic heterogeneous photonic layouts with optimal film quality, for hatching advanced optoelectronic applications and studying physical couplings among various functional nanomembranes[9,19,20,61].

Figures

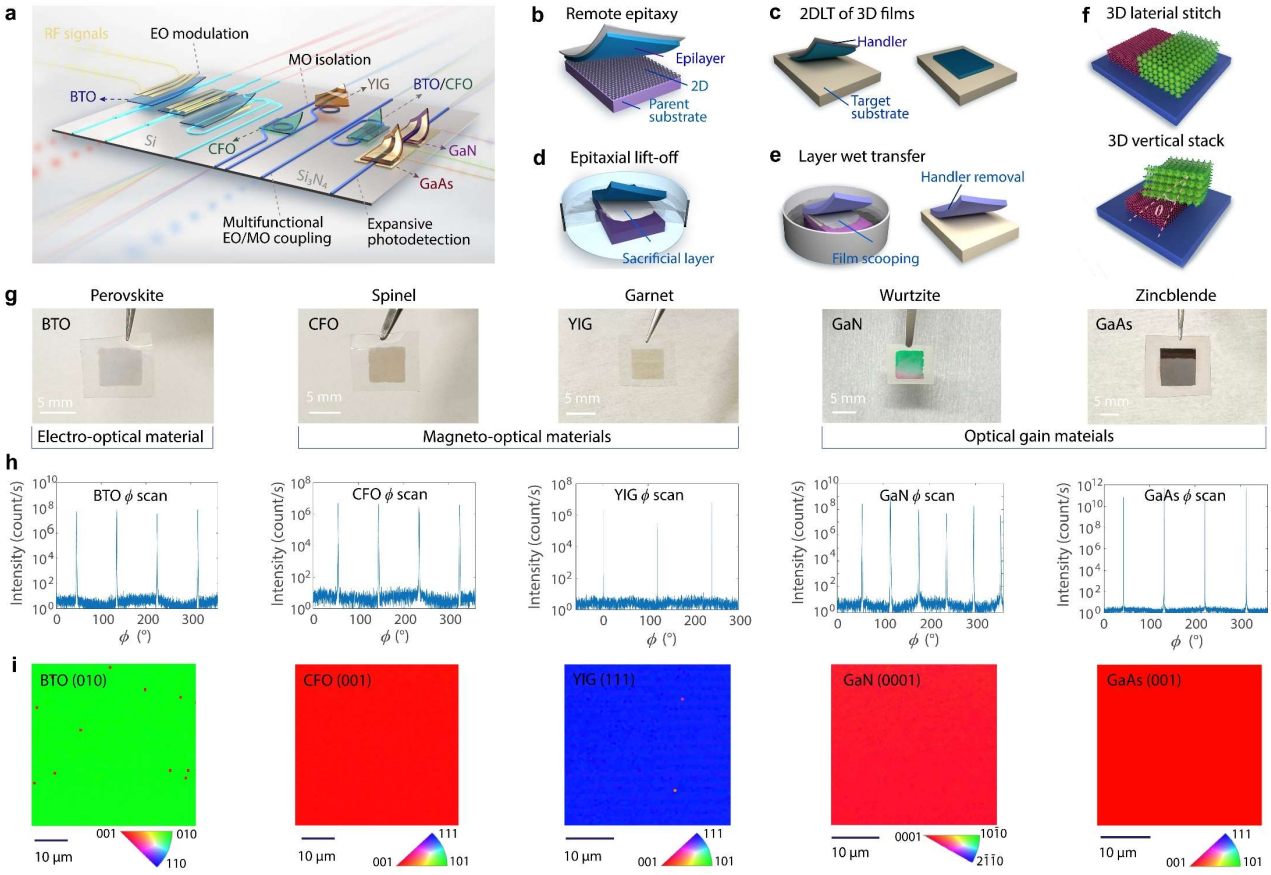


Figure 1. **Single-crystalline functional nanomembranes for photonic vdW integration**. (a) Infusing desired optical functionalities to Si and SiN photonics via vdW integration[11], such as EO modulation, MO isolation, and wide-spectrum photodetection. (b) Remote epitaxy[12,56] through 2D materials facilitates the release of single-crystalline epilayers. (c) 2DLT of freestanding 3D nanomembranes[10,17]. (d) Epitaxial lift-off[8,36] for thin film materials. (e) Wet transfer of 3D nanomembranes. (f) Photonic vdW integration modes: vertical stacking with optional rotation angle[19] (top), or lateral stitching. (g) Photographs of delaminated functional 3D nanomembranes resting on supportive PDMS (for BTO, CFO, and YIG) or TRT (for GaN and GaAs) handlers. (h) and (i) Asymmetric XRD ϕ-scan (h) and the corresponding EBSD map (i), respectively, of the ELO BTO, ELO CFO, 2DLT YIG, 2DLT GaN, and ELO GaAs nanomembranes (Supplementary Note 1).

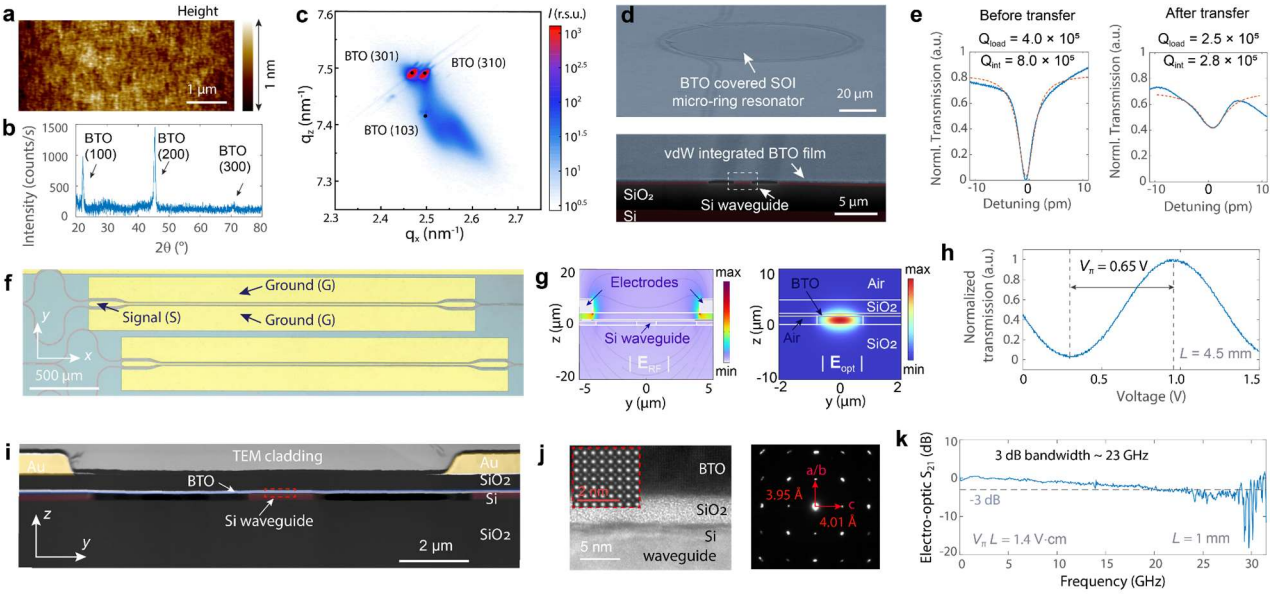


Figure 2. **Highly efficient EO modulation based on vdW integrating single-crystalline a-axis-domain BTO to Si photonics**.

(a) AFM of the as-grown BTO film surface. (b) 2θ-ω-scan XRD of freestanding a-axis-domain BTO on PDMS. (c) Reciprocal space map of thick BTO film transferred to fused silica, showing strong XRD signal intensity contrast between the dominant a-axis and negligible c-axis domains. I: intensity. r.s.u.: reciprocal space units. (d) Colored SEM image of a BTO-transferred SOI micro-ring: perspective- (top) and tilted cross-sectional-view (bottom). (e) Normalized optical transmission of a Si microring before (left panel) and after BTO transfer (right panel). Red dashed lines denote the Lorentzian fit of the spectral dip. Q_{int} and Q_{load}: intrinsic- and loaded-quality factors. (f) Optical micrograph of BTO-vdW integrated MZMs. (g) Simulated RF electric field (left), and the operating TE_0 mode optical field distributions (right) along the cross-section of a MZM arm. (h) Normalized optical transmission as a function of applied voltage for a 4.5-mm MZM device, with a low half-wave voltage of 0.65 V. (i) Colored cross-sectional SEM for the high-speed BTO/Si MZM. (j) Cross-sectional HR-TEM image showing BTO/Si waveguide interface (left panel) with dark-field STEM BTO lattice zoom-in (inset). Right panel: selected area electron diffraction from BTO region confirming a-axis-domain. (k) EO bandwidth of the high-speed BTO/Si MZM at 1.55 μm wavelength.

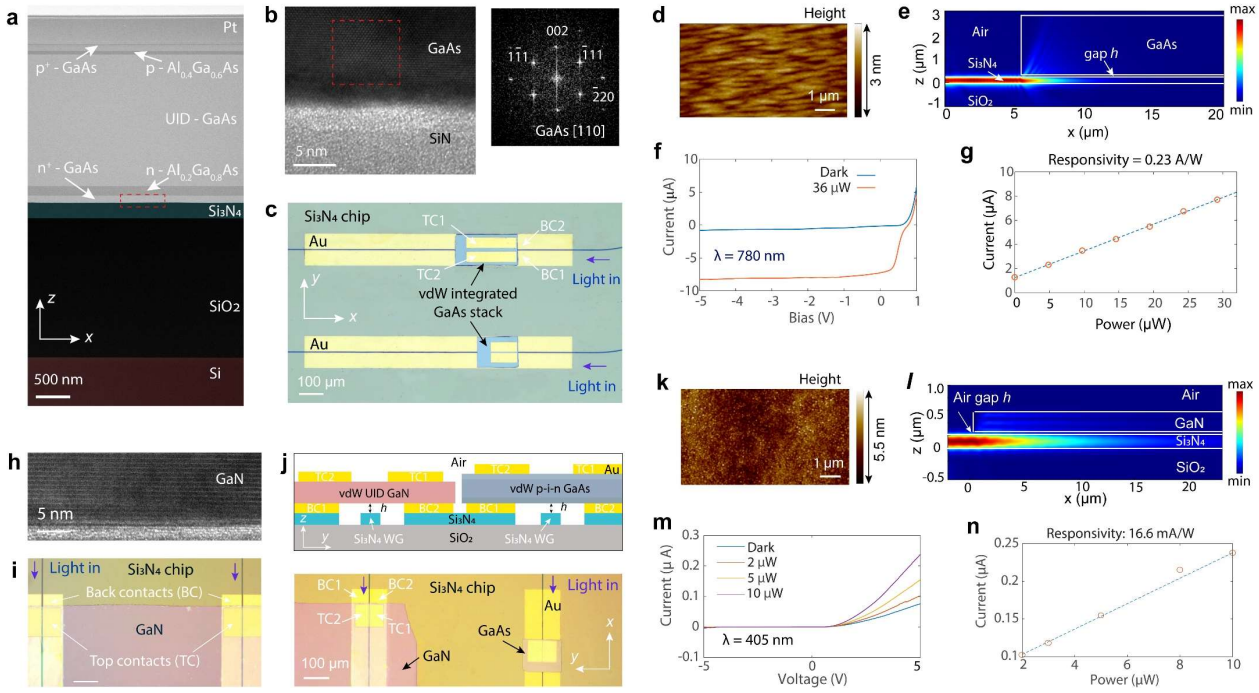


Figure 3. Expanding on-chip photodetection range by vdW integration of multiple III-V semiconductors on SiN photonics.

(a) Colored cross-sectional STEM image of the GaAs nanomembrane-transferred SiN chip, showing p-i-n doping structure of the epitaxial stacks. UID: unintentionally doped. (b) Left panel: HR-TEM image at the interface between vdW-integrated GaAs layer and SiN waveguide, showing GaAs lattice fringes. Right panel: TEM fast-Fourier-transform diagram of the highlighted n^+-GaAs area conforming [110] orientation. (c) Optical micrograph of the integrated GaAs Schottky photodetectors coupled to SiN waveguides. TC: top contact, BC: back contact. (d) AFM of the as-grown GaAs film surface. (e) Simulated light electric field $|\mathbf{E}_{\mathrm{opt}}|$ distribution along the photodetector cross-section, revealing efficient light absorption with air gap h ~30 nm. (f) Representative current-voltage (I-V) curve of the vdW-GaAs/SiN photodetector at different pump light intensities. (g) Fitted device photoresponsivity. (h) HR-TEM image of the GaN/SiN interface. (i) Optical micrograph of the vdW-integrated GaN/SiN photodetectors. (j) Top panel: Cross-sectional structure for the GaAs and GaN co-integrated photodetector. Bottom panel: Optical micrograph of the fabricated device. (k) AFM of the GaN film surface. (l) Simulated $|\mathbf{E}_{\mathrm{opt}}|$ distribution along the GaN/SiN photodetector longitudinal cross-section. (m) and (n) Representative I-V curves (m) and the corresponding photoresponsivity fit (n) of the photodetector, respectively.

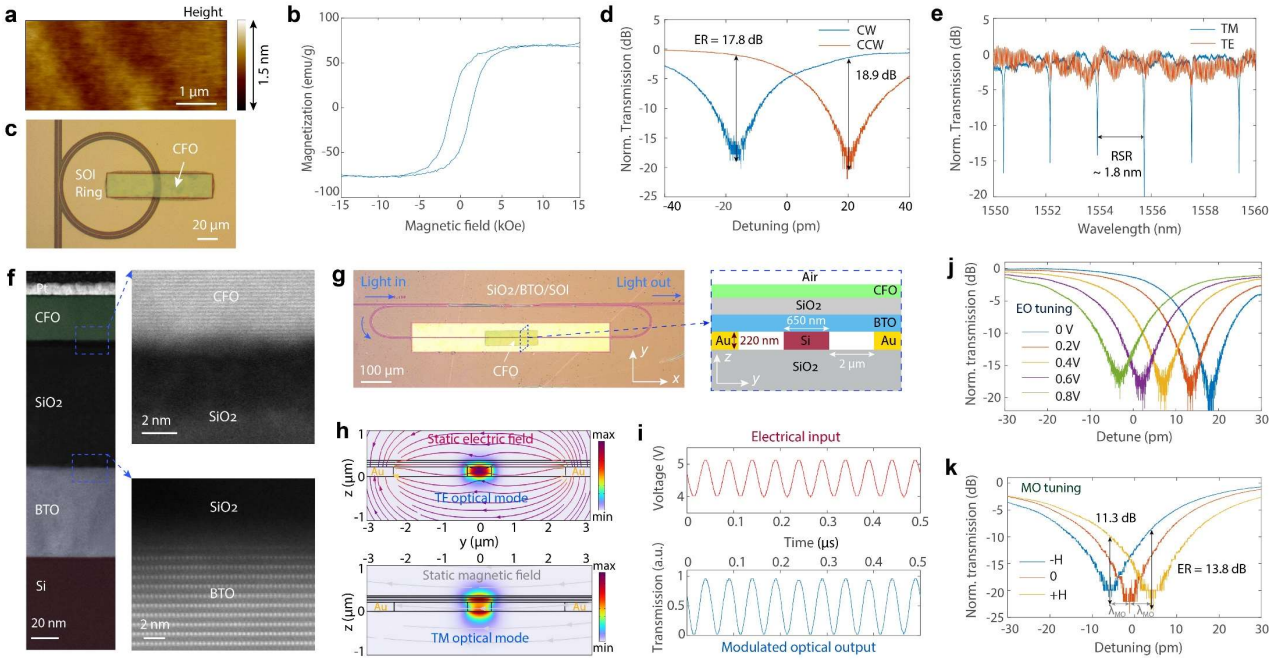


Figure 4. High-efficiency on-chip optical isolation and versatile electromagnetic coupling via CFO vdW integration.

(a) AFM of the as-grown CFO film surface. (b) CFO film ferromagnetic loop. (c) Optical micrograph of an optical isolator made by vdW integrating single-crystalline CFO film onto Si microring after lithographic patterning. (d) Normalized device non-reciprocal optical transmission for CW and CCW light measured under applied permanent magnet. ER: extinction ratio. (e) Normalized device optical transmission spectrum for fundamental TE and TM modes without external magnet. FSR: free spectrum range. (h) HR-STEM images of vertically stacked CFO/SiO_2/BTO/SOI heterostructures before CFO patterning, revealing single-crystalline CFO and BTO. (g) Left panel: Optical micrograph of the fabricated multifunctional EO and MO modulator. Right panel: Cross-sectional structure along the blue dashed plane in left panel. (h) Simulated static electric field distributions from buried electrodes for TE-mode EO modulation (top panel), and static magnetic field distributions from external neodymium magnet for TM-mode optical isolation (bottom panel). (i) EO modulation for the hybrid microring at 20 MHz applied voltage. (j) Microring resonant wavelength EO tuning under different applied voltage. (k) Same-device resonance wavelength MO tuning by reversing the external magnetic field direction.

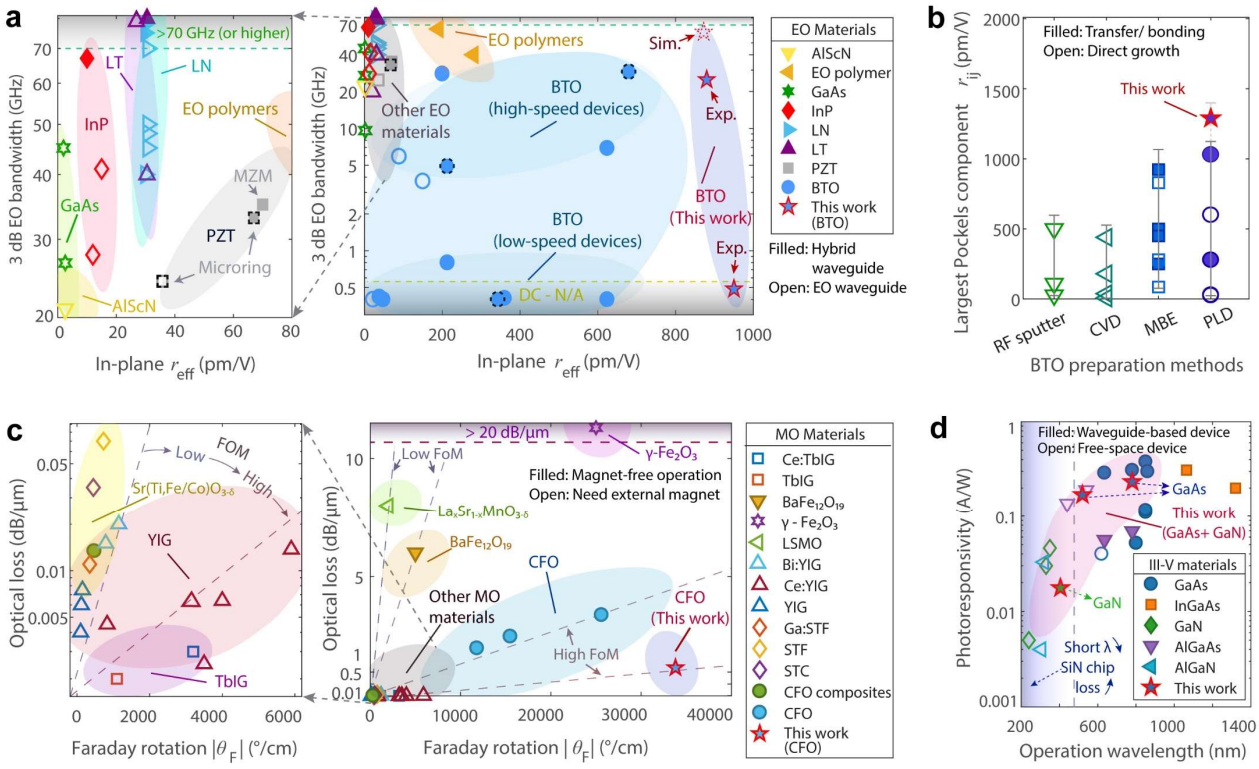


Figure 5. Performance benchmarks for vdW integrated photonic devices.

(a) EO performance benchmarks (right panel) and zoom-in view (left panel) of BTO to other EO materials. Solid profile: MZMs. Dashed profile: Microring modulators. Sim.: simulation. Exp.: experiment. DC-N/A: only direct-current or kHz EO tuning reported. (b) Benchmark of different BTO preparation methods. (c) MO performance benchmarks (right panel) and zoom-in (left panel) of CFO to other MO materials. Filled symbols: hard magnetic materials capable of magnet-less operations. Open symbols: soft magnetic materials. FoM: figure of merit. (d) Benchmarks of integrated photodetectors based on III-V materials.

References

1 Shi, Z. *et al.* Flat-panel laser displays through large-scale photonic integrated circuits. *Nature* **644**, 652-659 (2025).

2 Riemensberger, J. *et al.* A photonic integrated continuous-travelling-wave parametric amplifier. *Nature* **612**, 56-61 (2022).

3 Tran, M. *et al.* Extending the spectrum of fully integrated photonics. *Nature* **610**, 54–60 (2022).

4 Kaur, P. *et al.* Hybrid and heterogeneous photonic integration. *APL Photonics* **6**, 061102 (2021).

5 Shekhar, S. *et al.* Roadmapping the next generation of silicon photonics. *Nature Communications* **15**, 751 (2024).

6 Liu, Y., Huang, Y. & Duan, X. Van der Waals integration before and beyond two-dimensional materials. *Nature* **567**, 323-333 (2019).

7 Kum, H. S. *et al.* Heterogeneous integration of single-crystalline complex-oxide membranes. *Nature* **578**, 75-81 (2020).

8 Rogers, J. A., Lagally, M. G. & Nuzzo, R. G. Synthesis, assembly and applications of semiconductor nanomembranes. *Nature* **477**, 45-53 (2011).

9 Zhang, X. *et al.* Atomic lift-off of epitaxial membranes for cooling-free infrared detection. *Nature* **641**, 98-105 (2025).

10 Choi, C. *et al.* Reconfigurable heterogeneous integration using stackable chips with embedded artificial intelligence. *Nature Electronics* **5**, 386-393 (2022).

11 Meng, Y. *et al.* Photonic van der Waals integration from 2D materials to 3D nanomembranes. *Nature Reviews Materials* **8**, 498–517 (2023).

12 Kim, H. *et al.* Remote epitaxy. *Nature Reviews Methods Primers* **2**, 1-21 (2022).

13 Kim, B., Kim, M., Li, B. D., Hool, R. D. & Lee, M. L. Cryogenic GaAs laser power converters. *Solar Energy Materials and Solar Cells* **281**, 113321 (2025).

14 Kim, H. *et al.* High-throughput manufacturing of epitaxial membranes from a single wafer by 2D materials-based layer transfer process. *Nature Nanotechnology* **18**, 464-470 (2023).

15 Kong, W. *et al.* Polarity governs atomic interaction through two-dimensional materials. *Nature Materials* **17**, 999-1004 (2018).

16 Kim, H. *et al.* Graphene nanopattern as a universal epitaxy platform for single-crystal membrane production and defect reduction. *Nature Nanotechnology* **17**, 1054-1059 (2022).

17 Shin, J. *et al.* Vertical full-colour micro-LEDs via 2D materials-based layer transfer. *Nature* **614**, 81-87 (2023).

18 Bae, S.-H. *et al.* Integration of bulk materials with two-dimensional materials for physical coupling and applications. *Nature Materials* **18**, 550-560 (2019).

19 Sánchez-Santolino, G. *et al.* A 2D ferroelectric vortex pattern in twisted BaTiO3 freestanding layers. *Nature* **626**, 529-534 (2024).

20 Sun, H. *et al.* Ferroelectric topologies in BaTiO3 nanomembranes for light field manipulation. *Nature Nanotechnology* **20**, 881-888 (2025).

21 Shu, H. *et al.* Microcomb-driven silicon photonic systems. *Nature* **605**, 457-463 (2022).

22 Liang, D. & Bowers, J. E. Recent progress in heterogeneous III-V-on-silicon photonic integration. *Light: Advanced Manufacturing* **2**, 59-83 (2021).

23 De Koninck, Y. *et al.* GaAs nano-ridge laser diodes fully fabricated in a 300-mm CMOS pilot line. *Nature* **637**, 63-69 (2025).
24 Alexander, K. *et al.* A manufacturable platform for photonic quantum computing. *Nature* **641**, 876-883 (2025).
25 Bae, S.-H. *et al.* Graphene-assisted spontaneous relaxation towards dislocation-free heteroepitaxy. *Nature Nanotechnology* **15**, 272-276 (2020).
26 Smit, M., Williams, K. & Van Der Tol, J. Past, present, and future of InP-based photonic integration. *APL Photonics* **4**, 050901 (2019).
27 Zhu, D. *et al.* Integrated photonics on thin-film lithium niobate. *Advances in Optics and Photonics* **13**, 242-352 (2021).
28 Boes, A. *et al.* Lithium niobate photonics: Unlocking the electromagnetic spectrum. **379**, eabj4396 (2023).
29 Wang, C. *et al.* Integrated lithium niobate electro-optic modulators operating at CMOS-compatible voltages. *Nature* **562**, 101-104 (2018).
30 He, M. *et al.* High-performance hybrid silicon and lithium niobate Mach–Zehnder modulators for 100 Gbit s− 1 and beyond. *Nature Photonics* **13**, 359-364 (2019).
31 Yu, M. *et al.* Integrated femtosecond pulse generator on thin-film lithium niobate. *Nature* **612**, 252-258 (2022).
32 Feng, H. *et al.* Integrated lithium niobate microwave photonic processing engine. *Nature* **627**, 80-87 (2024).
33 Wang, C. *et al.* Lithium tantalate photonic integrated circuits for volume manufacturing. *Nature* **629**, 784-790 (2024).
34 Zhang, J. *et al.* Ultrabroadband integrated electro-optic frequency comb in lithium tantalate. *Nature* **637**, 1096-1103 (2025).
35 Castellanos-Gomez, A. *et al.* Van der Waals heterostructures. *Nature Reviews Methods Primers* **2**, 58 (2022).
36 Kum, H. *et al.* Epitaxial growth and layer-transfer techniques for heterogeneous integration of materials for electronic and photonic devices. *Nature Electronics* **2**, 439-450 (2019).
37 Han, S. *et al.* High energy density in artificial heterostructures through relaxation time modulation. *Science* **384**, 312-317 (2024).
38 Pintus, P. *et al.* Integrated non-reciprocal magneto-optics with ultra-high endurance for photonic in-memory computing. *Nature Photonics* **19**, 54-62 (2025).
39 Bi, L. *et al.* On-chip optical isolation in monolithically integrated non-reciprocal optical resonators. *Nature Photonics* **5**, 758-762 (2011).
40 Pintus, P. *et al.* An integrated magneto-optic modulator for cryogenic applications. *Nature Electronics* **5**, 604-610 (2022).
41 Ramirez, J. M. *et al.* III-V-on-Silicon Integration: From Hybrid Devices to Heterogeneous Photonic Integrated Circuits. *IEEE Journal of Selected Topics in Quantum Electronics* **26**, 1-13 (2020).
42 Chelladurai, D. *et al.* Barium titanate and lithium niobate permittivity and Pockels coefficients from megahertz to sub-terahertz frequencies. *Nature Materials* **24**, 868-875 (2025).
43 Abel, S. *et al.* Large Pockels effect in micro-and nanostructured barium titanate integrated on silicon. *Nature Materials* **18**, 42-47 (2019).

44 Messner, A. *et al.* Plasmonic Ferroelectric Modulators. *J. Lightwave Technol.* **37**, 281-290 (2019).
45 Eltes, F. *et al.* An integrated optical modulator operating at cryogenic temperatures. *Nature Materials* **19**, 1164-1168 (2020).
46 Abel, S. *et al.* A strong electro-optically active lead-free ferroelectric integrated on silicon. *Nature Communications* **4**, 1671 (2013).
47 Thureja, P. *et al.* Spalled Barium Titanate Single Crystal Thin Films for Functional Device Applications. *Nano Letters* **25**, 11089-11096 (2025).
48 Serrano-Núñez, M. A., Shoji, Y. & Mizumoto, T. Small magnetless integrated optical isolator using a magnetized cobalt ferrite film. *IEICE Electronics Express* **19**, 20210500-20210500 (2022).
49 Serrano-Núñez, M. A., Shoji, Y. & Mizumoto, T. J. A. P. E. Giant Faraday rotation of cobalt ferrite thin films deposited on silicon substrates for silicon photonic nonreciprocal device applications. *Applied Physics Express* **13**, 062002 (2020).
50 Sato, K., Okano, M. & Shoji, Y. Ultra-compact microring optical isolator using an aluminum-substituted cobalt ferrite thin film. *Optica* **11**, 889-895 (2024).
51 Lee, S. *et al.* Route to Enhancing Remote Epitaxy of Perovskite Complex Oxide Thin Films. *ACS Nano* **18**, 31225-31233 (2024).
52 Dötsch, H. *et al.* Applications of magneto-optical waveguides in integrated optics: review. *J. Opt. Soc. Am. B* **22**, 240-253 (2005).
53 Minemura, D. *et al.* Compact magneto-optical isolator by μ-transfer printing of magneto-optical single-crystal film on silicon waveguides. *Optics Express* **31**, 27821-27829 (2023).
54 Zhang, Y. *et al.* Monolithic integration of broadband optical isolators for polarization-diverse silicon photonics. *Optica* **6**, 473-478 (2019).
55 Jin, G. *et al.* Heteroepitaxial van der Waals semiconductor superlattices. *Nature Nanotechnology* **16**, 1092-1098 (2021).
56 Chang, C. S. *et al.* Remote epitaxial interaction through graphene. *Science Advances* **9**, eadj5379 (2023).
57 Kim, H. *et al.* Impact of 2D–3D Heterointerface on Remote Epitaxial Interaction through Graphene. *ACS Nano* **15**, 10587-10596 (2021).
58 Varshney, S. *et al.* Hybrid Molecular Beam Epitaxy for Single-Crystalline Oxide Membranes with Binary Oxide Sacrificial Layers. *ACS Nano* **18**, 6348-6358 (2024).
59 Yoon, J. *et al.* Heterogeneously Integrated Optoelectronic Devices Enabled by Micro-Transfer Printing. *Advanced Optical Materials* **3**, 1313-1335 (2015).
60 Huang, J.-K. *et al.* High-κ perovskite membranes as insulators for two-dimensional transistors. *Nature* **605**, 262-267 (2022).
61 Zhang, J. *et al.* Super-tetragonal Sr4Al2O7 as a sacrificial layer for high-integrity freestanding oxide membranes. *Science* **383**, 388-394 (2024).
62 Chiabrera, F. M. *et al.* Freestanding Perovskite Oxide Films: Synthesis, Challenges, and Properties. *Annalen der Physik* **534**, 2200084 (2022).
63 Narayan, J. & Larson, B. C. Domain epitaxy: A unified paradigm for thin film growth. *Journal of Applied Physics* **93**, 278-285 (2003).
64 Lisfi, A. *et al.* Reorientation of magnetic anisotropy in epitaxial cobalt ferrite thin films. *Physical Review B* **76**, 054405 (2007).

65 Jin, Z., Zhou, H., Zhang, X., Cao, K. & Chen, R. Interface-Mediated YIG/Ce:YIG Bilayers Structure with Enhanced Magneto-optical Properties via Pulsed Laser Deposition. *ACS Materials Letters* **5**, 803-810 (2023).
66 Boyd, R. W. in *Nonlinear Optics* 511-523 (Springer, 2008).
67 Karvounis, A., Timpu, F., Vogler-Neuling, V. V., Savo, R. & Grange, R. BaTiO3: Barium Titanate Nanostructures and Thin Films for Photonics *Advanced Optical Materials* **8**, 2070094 (2020).

Methods

1. Thin films growth

BTO

Single-crystalline (100) STO ($SrTiO_3$) substrates (sizes ranging from 10×10 mm square to 1″-diameter wafer, MSE Supplies) were first cleaned by acetone, isopropanol (IPA, ultrasonic bath), and then buffered oxide etchant (BOE, 6:1, over 30 seconds) to remove native oxide, followed by deionized (DI) water rinsing. STO substrates were then loaded to pulsed laser deposition (PLD, Rocky Mountain Vacuum Tech. Inc.) chamber for thermal annealing at 900 °C for 1 hour. SAO ($Sr_3Al_2O_6$) sacrificial layer[37,61,68-70] was grown around 800 °C under high vacuum condition (~10^{-6} Torr) for 6~10 min using a KrF excimer laser (wavelength $\lambda = 248$ nm, COMPex 205F, Coherent Inc.) with a 1 Hz repetition frequency and laser pulse energy (LPE) of 500 mJ. An ultrathin MgO (thickness < 1 nm) was shortly grown atop SAO to promote tensile BTO epitaxial strain relaxation[46,71] towards a-axis-domain (i.e. crystallographic c-axis parallel to film plane) BTO ($BaTiO_3$). BTO epitaxy was then performed at 120 mTorr O_2 pressure and 10 standard cubic centimeters per minute (sccm) O_2 flow for 2 Hz laser frequency and 500 mJ LPE, with varying growth time (5 ~ 20 min) and temperature (800~850 °C) depending on desired film thickness. In situ slow temperature ramping and annealing (900 °C) at high O_2 pressure were performed for over 3 hours, followed by another slow cooling process to minimize film stress[72,73] (Supplementary Note 4).

CFO

Single-crystalline (100) MgO substrates (10×10 mm square, MSE Supplies) were cleaned with similar steps to STO. After annealing at 900 °C in high-vacuum PLD chamber for 1 hour, a thin MgO sacrificial layer is homoepitaxially grown under 700 °C low O_2 pressure (10~20 mTorr, 6 sccm O_2 flow) for comparatively faster etching speed than substrate in weak acid solution. Under 500 mJ LPE and 5 Hz laser frequency, growth time varies from 20 ~ 30 minutes to get thin MgO buffer layer thickness around 20~30 nm. CFO ($CoFe_2O_4$) domain epitaxy[74] was then performed[64,75,76] at 750 °C (350 mJ LPE, 4 Hz frequency), 80 mTorr O_2 pressure (10 sccm flow) for ~5 min growth time, followed by in situ annealing for 30 min. Later, CFO epitaxy continued at similar condition (700 °C, 300 mJ LPE) with varying growth time to get desired film thickness. Post-growth annealing was performed for over 2 hours, followed by a slow cooling process.

YIG

For 2DLT YIG ($Y_3Fe_5O_{12}$), epitaxial monolayer graphene (Gr) was grown via silicon sublimation from the silicon face of 6H (0001) silicon carbide (SiC) in a three-phase graphite furnace (Thermal Technology LLC) detailed elsewhere[7]. Gr was then transferred to pre-cleaned single-crystalline (111) GGG ($Gd_3Ga_5O_{12}$) substrates via a semi-dry transfer method[12,77] (Supplementary Note 1) utilizing sputtered (via physical vapor deposition/PVD tool, Rocky Mountain Vacuum Tech. Inc.) stress-engineered (sputter chamber pressure: ~1×10^{-3} torr, Ar flow: 8 sccm) nickel (Ni, 99.99% purity) adhesive layer and thermal release tape (TRT). Remote epitaxy was performed on different 2D-coated growth templates with varying film exfoliation yield[51] (Supplementary Note 5). A thin YIG layer (<10 nm for 1500~2000 laser shots) was grown at 600 °C in Ar-rich (10 mTorr) PLD chamber to protect 2D, followed by normal YIG epitaxy at 700 °C (100 mTorr O_2 pressure, 10

sccm flow) to reach desired film thickness (500 mJ LPE, 10 Hz/2.92 W). Short post-growth annealing was performed at high O_2 pressure to improve crystal quality[7].

For ELO Ce: YIG ($Ce_1Y_2Fe_5O_{12}$), single-crystalline (100) MgO substrates were cleaned and then annealed at 900 °C in PLD chamber for 1 hour, followed by MgO[78] sacrificial layer epitaxy (similar to that for CFO). A thin YIG layer was then grown[65] at 850 °C (450 mJ LPE, 1 Hz laser frequency, 100 mTorr O_2 pressure) for 3 minutes and annealed for 2 hours, followed by continued Ce: YIG growth (400 mJ LPE, 2 Hz laser frequency, 120 mTorr O_2 pressure) before reaching desired film thickness. Upon completion, another in situ annealing is performed at 900 °C at high O_2 pressure for over 2 hours with a slow cooling process later.

GaN

Remote-epitaxial GaN films and in-situ BN (as epitaxy interlayer) and were grown in a Veeco Gen200 plasma-assisted molecular beam epitaxy (MBE) system[14]. Unintentionally doped (UID) GaN-on-sapphire (0001) wafers (4 μm-thick n-type GaN on 430-μm-thick single-side polished sapphire; MSE Supplies) were used as substrates. Prior to loading, the substrates were sequentially cleaned in acetone (60 °C, 15 min) and IPA (60 °C, 15 min), followed by N_2 blow-drying. They were then immersed in diluted HCl (33 vol% in DI water) for 15 min, rinsed with DI water, and blow-dried with nitrogen immediately before transferring to the MBE chamber. After pumping down to a base pressure of ~1×10^{-9} Torr using a cryogenic high-vacuum pump, the substrate temperature was ramped to 830 °C and held for 5 min to remove surface oxides and desorb residual contaminants. BN (nominal thickness 2–3 nm) was deposited at 830 °C for 45 min using a high-temperature boron effusion source and a plasma-assisted nitrogen source under nitrogen-rich conditions, with an operational chamber pressure of ~2×10^{-5} Torr (maintained during subsequent GaN growth).

Following BN growth, the substrate temperature was increased to 850 °C for GaN deposition. A ~30 nm GaN nucleation layer was first deposited under N_2-rich conditions for 10 min, using a high-temperature gallium effusion source and a plasma-assisted nitrogen source. The gallium flux was then increased to establish Ga-rich conditions, which promote lateral growth and facilitate film coalescence. This growth continued for 50 min, yielding a ~300 nm remote-epitaxial GaN film on top of the BN.

GaAs

For ELO GaAs, the GaAs film with p-i-n doping layers for photodetector was grown using a Veeco Mod Gen II solid-source MBE system[13,79]. A (001) semi-insulating GaAs substrate was first loaded and deoxidized at 660 °C for 30 minutes. A GaAs buffer layer was then deposited at a nominal GaAs growth temperature of 610 °C to bury any surface defects and obtain a smooth surface. A 200-nm-thick $Al_{0.9}Ga_{0.1}As$ sacrificial layer was grown to facilitate the ELO process. The device layers consist of n^+-GaAs contact, n-AlGaAs, intrinsic absorber, p-AlGaAs, and p^+-GaAs contact from the substrate to the surface. Si and Be were used as n- and p-dopants, respectively. For 2DLT GaAs, monolayer graphene-coated (001) single-crystal substrate is used for metal-organic chemical vapor deposition (MOCVD) with growth details elaborated in previous publications[12,77,80]. Given the complexity in optimizing remote epitaxial GaAs with desired doping structures[56], ELO GaAs is selected for photodetector demonstration.

2. Freestanding films lift-off and transfer

2D-materials-assisted layer transfer[10,17,18] (2DLT, Supplementary Fig. S1) and epitaxial lift-off[8,36] (ELO) were employed (Supplementary Figs. S2, S3), for producing single-crystalline freestanding nanomembranes to circumvent the heteroepitaxial constraints[81] prohibiting the creation of arbitrary heterogeneous photonic integration layouts via direct growth[11]. Different handler layers were tested, including polypropylene carbonate (PPC), poly methyl methacrylate (PMMA), ethylene-vinyl acetate (EVA), polydimethylsiloxane (PDMS), with different Young's modulus (see Ref.[82]), and thermal release tape (TRT). Overall, PPC was found effective for most ELO film transfer, and TRT-combined with Ni adhesive (and stressor) layer was found effective for most 2DLT cases (Supplementary Note 1).

2DLT

Ni stressor layer sputtering (1~2×10^{-3} torr pressure, Ar flow: 8 sccm) was first conducted for as-grown samples. By engineering sputtering conditions (chamber pressure), different Ni film stress levels can be achieved to assist film exfoliation[83]. If stronger stressor layer was needed to promote film delamination, a thin Ti adhesive layer (20~80 nm) would be deposited using electron-beam evaporation (PVD, Rocky Mountain Vacuum Tech. Inc.) before Ni sputtering with increased chamber pressure. TRT was then applied to the samples to mechanically exfoliate the whole stack including epilayer from substrate. Except for high-stressor layer applied cases such as GaN (Supplementary Note 15), the whole stack (TRT/stressor/epilayer) was then transferred to target substrate by pressing and rubbing with sponge swabs to ensure uniform contact[12,77]. TRT and Ni stressor layer were subsequently removed by hotplate baking (110~150 °C depending on TRT type) and $FeCl_3$ wet etching respectively. Repeated DI water rinsing, acetone, IPA, and O_2 plasma (PE 50 Asher, Plasma Etch Inc.) cleaning[14] were performed to remove process residues.

ELO

Polymer handler was first spin coated on as-grown samples followed by hotplate baking at varying temperatures depending on different polymers (Supplementary Note 1). Polymers at sample edges and backsides were removed by blade to ensure sufficient contact between the sacrificial layer and etchant, when floating the sample on the surface of the solution. For BTO, SAO sacrificial layer was dissolved in DI water[37]; For CFO[84] and YIG, MgO was etched by diluted acetic acid or ammonium sulfate ($(NH_4)_2SO_4$) aqueous solution; For ELO GaAs[13,79], AlAs sacrificial layer was etched by BOE (6:1) or diluted HCl. Upon lift-off completion, the nanomembranes were scooped onto target photonic templates for overnight drying up[36]. Soft hotplate baking (85~110 °C) is applied overnight to enhance nanomembranes bonding to the substrate (Supplementary Note 26). Polymer handlers were then removed by anisole, Remover PG (Kayaku Advanced Materials, Inc.), acetone, IPA, and DI water, with optional O_2 plasma cleaning to eliminate polymer residues.

3. Film quality characterizations

XRD

Grown samples were first characterized by quick 2θ-ω X-ray diffraction (XRD) scanning (Rigaku, MiniFlex XRD system) for initial crystal quality confirmation. High-resolution XRD ϕ-scans were collected on selected samples via a Bruker D8 Advance Diffractometer using Cu Kα radiation

($\lambda = 1.5406$ Å, operated at 40 kV, 40 mA) with line focus high-resolution configuration with a Ge (004) monochromator (channel cut configuration) in the primary optics. 2θ-ω symmetric scan XRD was first conducted to identify the peak position (out-of-plane 2θ-ω position). Then, the sample was tilted to the theoretical φ-scan angle, with corresponding angles calculated from the symmetric 2θ-ω scan. The φ-scan crystal plane/χ-tilting angle/2θ-ω positions for different materials were determined as: BTO (110)/45.0° /31.5 °, CFO (440)/45.0° /62.8 °, YIG (111)/ 70.5° / 51.0 °, GaN (102)/43.2° /48.1 °, GaAs (220)/45.0° /45.3 ° in XRD measurements. For BTO 2θ-ω XRD (Fig. 2b, and Supplementary Note 2), these a-axis-domain BTO exhibit slightly bigger XRD peak-angle positions than c-axis-domains (with the longer crystallographic c-axis perpendicular to film and the two shorter a-axes parallel to film plane)[43,46].

RSM

Reciprocal space mapping (RSM) scans were collected on the same Bruker D8 Advance Diffractometer. BTO samples were aligned to the (002) symmetric reflection; asymmetric RSM scans were acquired at (103) plane with low angle of grazing incidence with 1D scan mode. The ω,2θ grids were converted to reciprocal coordinates (q_x, q_z) using LEPTOS with the standard instrument geometry after tool calibrations (extended data and discussions in Supplementary Note 8).

SEM, EDS, and EBSD

Scanning electron microscopy (SEM), energy-dispersive X-ray spectroscopy (EDS, data shown in Supplementary Notes 3, 13, 16), and electron backscatter diffraction (EBSD) maps were measured by a Thermofisher Quattro S ESEM (equipped with Oxford symmetry electron backscattered detector) and a ZEISS Merlin high-resolution SEM (with EBSD detector). Environmental pressure operation (in ESEM) was adopted for less conductive substrates (as-grown film samples). EBSD maps were then collected with a 70° sample tilt angle and ~100% hit rate at varying acceleration voltages (10~30 kV).

AFM

Samples surface morphology characterizations were characterized via a Cypher S atomic force microscope (AFM, Asylum Research, Oxford Instruments) operated in tapping mode in ambient condition. Silicon tapping probes Titan 70 (Oxford Instruments, nominal resonance ~70 kHz, nominal spring constant ~2 $N \cdot m^{-1}$, and with Al backside coating) were driven near the cantilever resonance using piezo-acoustic base excitation. The cantilever resonance was determined by an auto-tune frequency sweep before imaging. During scanning, the amplitude setpoint was maintained at 70~80% of the free oscillation amplitude to minimize tip-sample forces while preserving stable tapping.

TEM & STEM

Thin samples for transmission electron microscopy (TEM) were prepared via a Thermofisher Scios2 FIB-SEM using a lift out method. High-resolution TEM images and selected area electron diffraction patterns were taken by a JEOL 2100F (S)TEM equipped with a Bruker EDS spectrometer and Gatan image filter.

The cross-sectional specimens BTO and CFO for scanning transmission electron microscopy (STEM) analysis were prepared using a FEI Helios Nanolab 600 Dual Beam System. Protective

layers of carbon (C) and subsequently platinum (Pt) were deposited over the BTO or CFO region using the electron beam to minimize ion-beam-induced damage during focused ion beam (FIB) milling. A lamella was then extracted from the region of interest using Ga^+ ion milling, lifted out with an Omniprobe nanomanipulator, and mounted onto a copper TEM half grid (Ted Pella). Final thinning was performed using low-energy Ga^+ ions. High-resolution imaging was conducted using an aberration-corrected STEM (Thermo Fisher Themis Z G3) operated at 200 kV. The probe convergence angle of 18.9 mrad, beam current 50 pA, and the image frame size 1024 × 1024 pixels with a 500 ns/pixel dwell time was used. A series of 15-20 frames were acquired and drift-corrected using the drift correction frame integration (DCFI) function in the Velox software to enhance the signal-to-noise ratio and obtain atomically resolved images of the BTO/CFO interface.

4. Si and SiN photonics fabrications

Si and SiN photonic chips were first designed and verified by electromagnetic numerical simulations (Ansys Lumerical FDTD Solutions, and COMSOL Multiphysics). Cleanroom nanofabrications were performed to create designed photonic structures based on commercial silicon-on-insulator (SOI, from UniversityWafer, Inc., and WaferPro, Inc.) or stoichiometric silicon nitride (Si_3N_4)-on-insulator (SiNOI) wafers. To achieve reduced Si waveguide (WG) height (such as the width×height as 1 μm×120 nm WG for Figs. 2g & 2h, and the 1.5 μm×150 nm WG for Fig. 2k), SOI wafers (original 220 nm device layer thickness) were first annealed at 1100 °C (via Lindberg tube furnace at ambient gas) for 2~3 hours (excluding ramping and cooling time) for Si surface oxidization. The resultant wafers were put into BOE (6:1) for surface SiO_2 removal to get desired SOI with reduced top Si-layer-thickness by controlling annealing time.

The diced SOI or SiNOI wafers (via Disco DAD323 dicing saw) were first cleaned by acetone and IPA (ultrasonic bath, then N_2 dry up), and spin coated with positive electron beam resist (ZEP520A, Zeonrex Electronic Chemicals Co.) with soft baking (180 °C, 3 minutes). For SiN samples, anti-charging agent (DisCharge H2OX2, DisChem, Inc.) was also spin coated later. Electron beam lithography (EBL, by Elionix ELS-S50EX) was then conducted (proximity effect-corrected). After resist development and pattern quality confirmation with optical microscopes, inductively coupled plasma reactive ion etching (ICP RIE, Oxford Plasma Lab 100) was applied, followed by Remover PG (Kayaku Advanced Materials, Inc.) boiling, acetone, IPA, and O_2 plasma cleaning for resist removal. For devices with buried electrodes structures such as the device in Fig. 4g, the area for electrodes was prepatterned and dry etched together with the waveguides (Supplementary Note 9). Thus, after electrodes formation (thermal evaporator, Edwards Auto 306 Vacuum Coater) and lift-off, the gold (with ~5 nm Ti adhesion layer) electrodes and the waveguides can have the same height to ensure good subsequent vdW integration yield and tight layer bonding.

The fabricated Si and SiN chips were tested by an edge-coupling setup. A tunable narrow-linewidth laser (New Focus TLB) was coupled to the as-cleaved waveguide sample via a fiber lens (OZ Optics Ltd.). The output light was collected by another fiber lens and fed to a photodetector (Newport 1811) with signals monitored by an oscilloscope (Rigol DS7054).

5. Pockels coefficient estimation

In anisotropic electro-optical (EO) crystals such as BTO[42], LN[27], and LT[33], their refractive indices can be described by the optical indicatrix $\mathbf{t}^T\boldsymbol{\eta}\mathbf{t} = 1$, where $\mathbf{t} = [x, y, z]^T$ is a real-space unit vector and $\boldsymbol{\eta}$ is the impermeability tensor[66]. This equation yields to the index ellipsoid: $\eta_1 x^2 + \eta_2 y^2 + \eta_3 z^2 + 2\eta_4 yz + 2\eta_5 zx + 2\eta_6 xy = 1$. Under applied static or RF electric field $\mathbf{E}_{\mathrm{RF}} = [E_x^{\mathrm{RF}}, E_y^{\mathrm{RF}}, E_z^{\mathrm{RF}}]^T$, the EO material's impermeability tensor is changed as $\boldsymbol{\eta}(\mathbf{E}_{\mathrm{RF}}) = \boldsymbol{\eta}(0) + \Delta\boldsymbol{\eta}(\mathbf{E}_{\mathrm{RF}})$, where $\boldsymbol{\eta}(0)$ is the zero-field (without applied electric field) impermeability tensor. Under Voigt notation[85], for Pockels (linear EO) effect, $\mathbf{E}_{\mathrm{RF}}$ induces linear change in $\Delta\boldsymbol{\eta}$ as

$$\begin{bmatrix}\Delta\eta_1\\ \Delta\eta_2\\ \Delta\eta_3\\ \Delta\eta_4\\ \Delta\eta_5\\ \Delta\eta_6\end{bmatrix} = \begin{bmatrix}\Delta(1/n^2)_1\\ \Delta(1/n^2)_2\\ \Delta(1/n^2)_3\\ \Delta(1/n^2)_4\\ \Delta(1/n^2)_5\\ \Delta(1/n^2)_6\end{bmatrix} = \mathbf{r}_{\mathrm{EO}} \cdot \mathbf{E}_{\mathrm{RF}} = \begin{bmatrix}r_{11} & r_{12} & r_{13}\\ r_{21} & r_{22} & r_{23}\\ r_{31} & r_{32} & r_{33}\\ r_{41} & r_{42} & r_{43}\\ r_{51} & r_{52} & r_{53}\\ r_{61} & r_{62} & r_{63}\end{bmatrix}\begin{bmatrix}E_x^{\mathrm{RF}}\\ E_y^{\mathrm{RF}}\\ E_z^{\mathrm{RF}}\end{bmatrix},$$

where $\Delta\left(\frac{1}{n^2}\right)_i$ with $i \in \{1,2,\dots,6\}$ describes the index change via the index ellipsoid deformation[85] under $\mathbf{E}_{\mathrm{RF}}$, r_{ij} are the components of Pockels tensor $\mathbf{r}_{\mathrm{EO}}$ (with $i \in \{1,2,\dots,6\}$, $j \in \{1,2,3\}$ under Voigt notation[66]). For BTO with $4mm$ symmetry, its Pockels tensor $\mathbf{r}_{\mathrm{BTO}}$ can be written as below[86], with $r_{51} = r_{42}$ and $r_{23} = r_{13}$.

$$\mathbf{r}_{\mathrm{BTO}} = \begin{bmatrix}0 & 0 & r_{13}\\ 0 & 0 & r_{23}\\ 0 & 0 & r_{33}\\ 0 & r_{42} & 0\\ r_{51} & 0 & 0\\ 0 & 0 & 0\end{bmatrix}$$

Set $\mathbf{e}_{\mathrm{opt}} = \mathbf{E}_{\mathrm{opt}}/|\mathbf{E}_{\mathrm{opt}}|$ is the unit polarization vector of operating optical eigenmode for EO modulations, where the altered mode index Δn is interested in. Under small EO perturbation, the change (first order) in the optical modes effective impermeability is the Rayleigh quotient[66] $\Delta\left(\frac{1}{n^2}\right) = \mathbf{e}_{\mathrm{opt}}^T\Delta\boldsymbol{\eta}\mathbf{e}_{\mathrm{opt}}$. Thus, the effective Pockels coefficient r_{eff} is denoted by integrating all rotation, tensor, and geometric factors into a scalar form

$$r_{\mathrm{eff}}E_{\mathrm{RF}} = \Delta\left(\frac{1}{n^2}\right) = \frac{\iint \mathbf{e}_{\mathrm{opt}}^T\Delta\boldsymbol{\eta}(\mathbf{t})\mathbf{e}_{\mathrm{opt}}|\mathbf{E}_{\mathrm{opt}}(\mathbf{t})|^2\,\mathrm{d}S}{\iint|\mathbf{E}_{\mathrm{opt}}(\mathbf{t})|^2\,\mathrm{d}S},$$

where $E_{\mathrm{RF}} = |\mathbf{E}_{\mathrm{RF}}|$, $\mathrm{d}S$ is the cross-sectional area element where the optical field $\mathbf{E}_{\mathrm{opt}}(\mathbf{t})$ and electric field $\mathbf{E}_{\mathrm{RF}}(\mathbf{t})$ varies along. Given that $\Delta\left(\frac{1}{n^2}\right) \approx -2\Delta n/n_{(0)}^3$, where Δn is the EO index change and $n_{(0)}$ is the unperturbed optical refractive index[42], r_{eff} can be estimated by $r_{\mathrm{eff}} = -\frac{2\Delta n}{n_{(0)}^3 E_{\mathrm{RF}}}$. The mode index change Δn and the BTO material index change can be connected[44,87] by $\Delta n = \Delta n_{\mathrm{BTO}} \cdot \Gamma$, where $\Gamma = \frac{\iint_{\mathrm{BTO}}\frac{1}{2}\Re(\mathbf{E}_{\mathrm{opt}}\times\mathbf{H}_{\mathrm{opt}}{}^*)\cdot\hat{\mathbf{x}}\,\mathrm{d}S}{\iint_{\mathrm{All}}\frac{1}{2}\Re(\mathbf{E}_{\mathrm{opt}}\times\mathbf{H}_{\mathrm{opt}}{}^*)\cdot\hat{\mathbf{x}}\,\mathrm{d}S}$ is the spatial overlap between the optical mode and the BTO film. At half-wave voltage V_π , the phase modulation is $-\pi = \frac{2\pi L}{\lambda}\Delta n$, by

approximating the applied electric field[88] as $E_{\mathrm{RF}} = \frac{V_\pi}{g}$, the effective Pockels coefficient can be estimated (detailed in Supplementary Note 6) by

$$r_{\mathrm{eff}} = \frac{\lambda g}{n_{(0)}^3 \Gamma V_\pi L},$$

where light wavelength $\lambda = 1.55$ μm, g is the electrodes distance (g =4 μm for MZM in Fig. 2h, g =8 μm for MZM in Fig. 2k), and L is device length. Taking BTO $n_{(0)}$ =2.26 (Refs.[42,66]), we have the estimated $r_{\mathrm{eff}} \approx 950$ pm/V. If take $n_{(0)}$ =2.27 (Refs.[43,87]), the updated estimation is $r_{\mathrm{eff}} \approx$ 928 pm/V. Roughly assuming[66] $r_{33} = 100$ pm/V, $r_{13} = 10$ pm/V, for $n_{(0)}$: 2.26~2.27, it corresponds to r_{42}: 1250 ~ 1290 pm/V. Realistic smaller r_{33} or r_{13} values will lead to bigger estimated r_{42}, under given optimal $r_{\mathrm{eff}} = \frac{\sqrt{2}}{4}(2r_{42} + r_{33} + r_{13})$ (Supplementary Notes 7), which highly depends on BTO crystallographic quality and c-axis orientation after BTO domain poling[72]. See Supplementary Notes 6, 11, 12 for further rigorous calculations and discussion details.

6. High-speed EO modulation

BTO poling[72,89] is vital for strong EO Pockels response[24,42]. After device fabrication, BTO was poled by applying a DC voltage around 20~80 V to electrodes (by Keithley 2450 SourceMeter, SMU) depending on film thickness, followed by repeated voltage sweepings at lower bias voltage ranges. For KHz- to MHz-level (voltage frequency) initial EO modulation tests, electrodes voltage signals were driven by function generator (Rigol DG4202, Function/Arbitrary Waveform Generator, 200 MHz). The voltage DC offsets (-10~10 V) are manually adjusted to find optimal EO responses (bias tee needed for high-frequency DC offsets). High-speed EO applications over GHz-level require travelling-wave electrodes with proper device structure, ideally satisfying (1) Z_0 =50 Ω device characteristic impedance, (2) matched microwave n_g^{RF} and optical mode group velocities n_g^{Opt}, and (3) low microwave loss. Electromagnetic simulations (via COMSOL Multiphysics) are performed accordingly (detailed in Supplementary Notes 10, 11).

For high-speed EO modulation, the optical carrier at 1550 nm from a tunable laser source (Toptica CTL) was amplified using an erbium-doped fiber amplifier (EDFA) to provide sufficient input power. A fiber polarization controller was employed to adjust and maintain the polarization state, ensuring efficient excitation of the fundamental TE mode in the waveguide. The amplified polarization-optimized light was coupled into the chip through a lensed fiber in an end-fire configuration, while the output was collected by another lensed fiber and directed to a high-speed photodiode (XPDV4120R) for optical-to-electrical conversion. On the electrical side, a pair of 67 GHz ground-signal-ground (GSG) microwave probes (GGB) delivered the RF signal from a vector network analyzer (VNA, R&S ZNA67) to the transmission line electrodes of the device under test, with the output terminated by a matched 50 Ω load to suppress reflections and maintain impedance matching. The detected signal from the high-speed photodiode was fed back into the VNA to obtain the electro-optic frequency response. The VNA was calibrated to the end of the cables using a standard through-open-short-match (TOSM) method with a coaxial calibration kit. The intrinsic EO response of the device was extracted by subtracting the independently measured response of the photodiode and the input probe from the recorded S_{21} (measured as ratio of powers, Supplementary Note 14).

7. III-V/SiN device fabrication and measurement

Given that 2DLT comparatively has more stringent requirements on template preparation and kinetic optimization[12,14,25] to obtain desired doping structures, ELO GaAs nanomembranes with designed positive-intrinsic-negative (p-i-n) doping heterostructures are adopted for enhanced photoresponsivity[13]. UID GaN nanomembranes were vdW integrated to prefabricated SiN chips (with bottom electrodes contacts) via 2DLT (detailed in Supplementary Note 15). Soft baking (~110 °C, overnight) was applied to enhance film adhesion before PPC polymer handler removal. The transferred ELO GaAs nanomembranes were then spin coated with thick PMMA combo (first 495-A11, then 950-A7, Kayaku Advanced Materials, Inc., both coated at 1500 rpm, 180 °C for 3 minutes baking applied after spin coating each PMMA layer), followed by EBL patterning (950 $\mu C/cm^2$ dose, at 10 nA current) and PMMA resist development. GaAs at exposed area (i.e. without top PMMA layer protection) were etched by mixed aqueous H_2SO_4 and H_2O_2 solution. GaN nanomembranes were not patterned in this work due to lacking satisfactory highly selective etchant. All the III-V devices can be further improved by employing optimized ICP-RIE patterning (Supplementary Note 17).

For photodetectors measurement, a 780 nm-wavelength laser (TLB-6712, MKS Newport Co.) with adjusted power and polarization was coupled to the GaAs-vdW integrated SiN waveguide photodetectors. Bias voltage and photocurrent measurements are completed through a source meter unit (SMU, Keithley 2450). When applying bias voltage, only one pair of electrodes (TC1 & BC1, or TC2 & BC2) were probed at one time. For short wavelengths (<500 nm), the optical loss of our home-made SiN chips evidently increased, calibrations were made to estimate the optical power fed into the GaN photodetectors[90] (Supplementary Note 16). Fiber-coupled single-mode laser diodes (LT-405030-SM-FC, LT-450025-SM-FC, and LT-520045-SM-FC, by Laser Tree Inc.) served as light sources of different wavelengths (405 nm, 450 nm, and 520 nm, respectively).

8. Nanomembrane lateral stitching and vertical stacking procedures

Lateral stitching of freestanding nanomembranes was implemented via optical microscope-assisted transfer, with sequential lithographical film patterning. For the GaAs and GaN co-integrated SiN photodetectors (Fig. 3j), GaAs layer was transferred and patterned first, followed by subsequent GaN transfer. For the vertical stacking of artificial 3D vdW heterostructures GaAs/BTO/GaN/STO atop SiO_2 substrate, single-crystalline STO (first), GaN, BTO, and GaAs (last) are sequentially wet transferred with PPC handler. After transferring a layer, overnight drying and soft baking (100 °C) were applied before PPC removal to enhance nanomembrane adhesion (Supplementary Note 3). Both lateral stitching (Supplementary Fig. S10b) and vertical stacking (Supplementary Fig. S10c) of these 4 freestanding nanomembranes (with distinct crystal structures: zincblende-GaAs, tetragonal perovskite-BTO, wurtzite-GaN, cubic perovskite-STO) were experimentally demonstrated (single-crystalline for each layer), which is hardly accessed by direct heteroepitaxy[7].

To pattern vertically stacked 3D nanomembranes heterostructures, such as the device in Fig. 2g, an 80 nm-thick SiO_2 was reposited by plasma-enhanced chemical vapor deposition (PECVD,

Oxford Nanofab Instrument) atop the entire sample after transferring the 60 nm-thick freestanding BTO, in order to protect the gold electrodes and BTO layer from later wet etching (Supplementary Note 19). Negative e-beam resist (ma-N 2400, Micro Resist Tech.) was spin coated to the sample after completing CFO nanomembranes transfer, followed by EBL patterning and development (ma-D 525, Micro Resist Tech.). Undesired CFO film areas were then wet etched and removed by a mixed (HCl, H_3PO_4, and H_2O_2 at 60 °C) solution. The one-inch-diameter freestanding BTO[82] (Supplementary Fig. S31) was transferred to SiO_2 substrate via PPC handler. The vdW integrated nanomembranes were found with high robustness and tight bonding to the substrates after proper thermal treatment, capable of withstanding moderate ultrasonic processes without delamination (Supplementary Note 26).

9. Faraday rotation coefficient estimation

Light propagating in magneto-optical (MO) materials such as CFO undergoes polarization rotation under external magnetic field[52]. The MO effect-induced change in the effective index of the operating mode Δn_{eff} (fundamental TM mode for our case) alters the resonance condition of the underlying Si microring resonator by

$$\Delta\lambda = \frac{\lambda \Delta n_{\mathrm{eff}}}{n_{\mathrm{g}}},$$

where $\Delta\lambda$ is the resultant wavelength shift, n_{g} is group velocity connected to the free spectrum range (FSR) by $\mathrm{FSR} \approx \frac{\lambda^2}{n_g L}$ (L is the microring perimeter). Given the experimentally measured FSR as 1.82 μm, wavelength split between CW and CCW light as $\Delta\lambda = 2\lambda_{\mathrm{MO}}$ ≈36 pm for device shown in Fig. 4d, the non-reciprocal phase shift can be estimated[91] as $\Delta\Phi_{\mathrm{NRPS}} = 2\pi\frac{\Delta\lambda}{\mathrm{FSR}} = 2{\theta_{\mathrm{F}}}^{\mathrm{eff}} L_{\mathrm{MO}}$, where ${\theta_{\mathrm{F}}}^{\mathrm{eff}}$ is the mode-effective Faraday rotation coefficient and $L_{\mathrm{MO}} \approx 26.5$ μm is the length of CFO-covered arc[92]. The CFO material Faraday rotation coefficient ${\theta_{\mathrm{F}}}^{\mathrm{film}}$ can thus be calculated by

$${\theta_{\mathrm{F}}}^{\mathrm{film}} = \frac{\Delta\Phi_{\mathrm{NRPS}}}{2L_{\mathrm{MO}}\Gamma},$$

where $\Gamma = \frac{\iint_{\mathrm{CFO}_2} \frac{1}{2}\Re(\mathbf{E}\times\mathbf{H}^*)\cdot\hat{\mathbf{x}}\,\mathrm{d}S}{\iint_{\mathrm{All}_2} \frac{1}{2}\Re(\mathbf{E}\times\mathbf{H}^*)\cdot\hat{\mathbf{x}}\,\mathrm{d}S}$ is the modal overlap factor between the operating mode and CFO film, with the relation[66] ${\theta_{\mathrm{F}}}^{\mathrm{film}} = {\theta_{\mathrm{F}}}^{\mathrm{eff}}/\Gamma$. Taking numerically simulated $\Gamma = 3.98\%$, the CFO film Faraday rotation coefficient is calculated as ${\theta_{\mathrm{F}}}^{\mathrm{film}} \approx 33800°/\mathrm{cm}$ (details in Supplementary Note 21).

10. Non-reciprocal transmission measurement

The optical transmission measurements were similar to the pre-characterizations of the fabricated Si and SiN waveguide samples via identical experimental setup (chip end-coupling with fiber lenses, function generators, photodetectors, and an oscilloscope). The input polarization was carefully adjusted via fiber polarization controller to excite TM mode, maximizing MO modulation

efficiency. After locating the resonant wavelength of the microring by adjusting the tunable laser wavelength, a strong neodymium magnet was then placed proximity to the sample via a mechanical clamp, ensuring the magnetic field was approximately parallel to the chip plane and perpendicular to the bus waveguide coupled to the microring[39,52]. The magnetic field intensity around the sample was found around 300 mT by a magnetometer. The CFO (Fig. 4b) and YIG ferromagnetic hysteresis loop (Supplementary Fig. S28) were calibrated by subtracting substrate response from measured as-grown sample, and then calculated by retrieving the estimated MO film mass (calculated by multiplying the film area size, thickness, and literature density) to obtain the magnetization emu/g (electromagnetic unit of magnetic moment per gram, Supplementary Note 22).

References (Methods)

68 Mengxue, T. *et al.* Towards high quality transferred barium titanate ferroelectric hybrid integrated modulator on silicon. *Light: Advanced Manufacturing* **5**, 479-489 (2024).

69 Pesquera, D., Fernández, A., Khestanova, E. & Martin, L. W. Freestanding complex-oxide membranes. *Journal of Physics: Condensed Matter* **34**, 383001 (2022).

70 Ji, J., Park, S., Do, H. & Kum, H. S. A review on recent advances in fabricating freestanding single-crystalline complex-oxide membranes and its applications. *Physica Scripta* **98**, 052002 (2023).

71 Lee, J. W. *et al.* In-plane quasi-single-domain BaTiO3 via interfacial symmetry engineering. *Nature Communications* **12**, 6784 (2021).

72 Wen, Y. *et al.* Enhanced Electro-Optic Coefficients in Single-Crystalline BaTiO3 Thin Films Enabled by Domain Alignment. *Advanced Optical Materials* **12**, 2303058 (2024).

73 Kim, B. *et al.* Controlling of lattice strains for crack-free and strong ferroelectric barium titanate films by post-thermal treatment. *Scientific Reports* **12**, 5363 (2022).

74 Zheleva, T., Jagannadham, K. & Narayan, J. Epitaxial growth in large-lattice-mismatch systems. *Journal of Applied Physics* **75**, 860-871 (1994).

75 Yanagihara, H., Uwabo, K., Minagawa, M., Kita, E. & Hirota, N. Perpendicular magnetic anisotropy in CoFe2O4(001) films epitaxially grown on MgO(001). *Journal of Applied Physics* **109**, 07C122 (2011).

76 Chambers, S. A. *et al.* Molecular beam epitaxial growth and properties of CoFe2O4 on MgO(001). *Journal of Magnetism and Magnetic Materials* **246**, 124-139 (2002).

77 Kim, Y. *et al.* Remote epitaxy through graphene enables two-dimensional material-based layer transfer. *Nature* **544**, 340-343 (2017).

78 Sung, S.-Y., Qi, X. & Stadler, B. J. H. Integrating yttrium iron garnet onto nongarnet substrates with faster deposition rates and high reliability. *Applied Physics Letters* **87**, 121111 (2005).

79 Chen, H. *et al.* Plasmonically Enhanced Spectral Upconversion for Improved Performance of GaAs Solar Cells under Nonconcentrated Solar Illumination. *ACS Photonics* **5**, 4289-4295 (2018).

80 Kim, H. *et al.* Role of transferred graphene on atomic interaction of GaAs for remote epitaxy. *Journal of Applied Physics* **130**, 174901 (2021).

81 Tan, C., Chen, J., Wu, X.-J. & Zhang, H. Epitaxial growth of hybrid nanostructures. *Nature Reviews Materials* **3**, 17089 (2018).

82 Moon, J.-Y. *et al.* Crack-Free Transfer of Wafer-Scale Freestanding Single-Crystalline Nanomembranes Enabled by Elastically Graded Polymer. *Advanced Materials*, e13080, (2025).
83 Shim, J. *et al.* Controlled crack propagation for atomic precision handling of wafer-scale two-dimensional materials. *Science* **362**, 665-670 (2018).
84 Salles, P. *et al.* Bendable Polycrystalline and Magnetic CoFe2O4 Membranes by Chemical Methods. *ACS Applied Materials & Interfaces* **14**, 12845-12854 (2022).
85 Hu, Y. *et al.* Integrated electro-optics on thin-film lithium niobate. *Nature Reviews Physics* **7**, 237-254 (2025).
86 Steglich, P. & Kehrein, A. Light propagation in anisotropic materials and electro-optical effects: tutorial on the use of eigenvalue problems, tensors, and symmetries. *J. Opt. Soc. Am. B* **41**, 2191-2210 (2024).
87 Eltes, F. *et al.* A BaTiO3-Based Electro-Optic Pockels Modulator Monolithically Integrated on an Advanced Silicon Photonics Platform. *J. Lightwave Technol.* **37**, 1456-1462 (2019).
88 Hu, X., Cueff, S., Romeo, P. R. & Orobtchouk, R. Modeling the anisotropic electro-optic interaction in hybrid silicon-ferroelectric optical modulator. *Optics Express* **23**, 1699-1714 (2015).
89 Nakao, O., Tomomatsu, K., Ajimura, S., Kurosaka, A. & Tominaga, H. Influence of 180° domains on ferroelectric properties of BaTiO3 single crystal. *Applied Physics Letters* **61**, 1730-1732 (1992).
90 Moun, M., Kumar, M., Garg, M., Pathak, R. & Singh, R. Understanding of MoS2/GaN Heterojunction Diode and its Photodetection Properties. *Scientific Reports* **8**, 11799 (2018).
91 Yan, W. *et al.* Ultra-broadband magneto-optical isolators and circulators on a silicon nitride photonics platform. *Optica* **11**, 376-384 (2024).
92 Dushaq, G., Serunjogi, S., Tamalampudi, S. R. & Rasras, M. Non-reciprocal response in silicon photonic resonators integrated with 2D CuCrP2S6 at short-wave infrared. *Light: Science & Applications* **14**, 157 (2025).

Data and code availability

All data from this study are included in the paper and are available from the corresponding author upon request.

Acknowledgements

S.-H.B. and L.Y. acknowledge support from National Science Foundation (grant No. 2428676). J.S. and H.K. acknowledge cleanroom support from Illinois Materials Research Science and Engineering Center (IMRSEC). Y.M., S.-H.B. and L.Y. thanks FIB assistance from Dr. Huafang Li at Washington University in St. Lous, and helpful discussions from Dr. Sangho Lee at Massachusetts Institute of Technology (MIT).

The samples were fabricated primarily in the cleanroom of Institute of Materials Science and Engineering (IMSE) at Washington University in St. Louis (WUSTL), and by part in Holonyak Micro & Nanotechnology Lab (HMNTL) at University of Illinois Urbana-Champaign (UIUC). Material characterizations were performed via facilities in IMSE at WUSTL, HMNTL at UIUC, and Microsystems Technology Laboratories (MTL) at MIT.

Author contributions

Y.M., S.-H.B., W.M., and L.Y. conceived the idea. Y.M. and W.M. designed the experiments. Y.M. performed PLD growth and layer lift-off for BTO, CFO, and YIG films with inputs from S.M., J.-Y.M., X.Z., and Y.C. B.K. performed the MBE growth of GaAs films with support from M.L.L. X.Z. performed the remote epitaxy and characterizations of YIG films with support from Jeehwan K. S.L. and Jekyung K. performed the MBE growth and exfoliation of BN and GaN films. Y.M. fabricated the Si and SiN photonic chips with inputs from W.M., Z.X., W.X., Q.Z., and S.H.C. Y.M. performed the vdW integration of nanomembranes to photonic chips. D.J. designed the travelling wave electrodes for EO modulators. Y.M. and W.M. measured the low-speed EO responses with input from D.J. and W.X. M.L. measured the microwave and high-speed EO modulation with support from J.H. and T.J.K. Y.M. and W.M. measured the MO non-reciprocal devices and photodetectors based on GaAs and GaN with inputs from D.J., and Z.X. J.S. performed XRD and RSM measurements with inputs from Y.M., S.R., and H.K. Y.M. performed SEM and EBSD for various samples. E.P. and X.H. performed the TEM, STEM, and EDS characterizations with support from F.M.R. S.H.N. performed ferromagnetic hysteresis measurements with inputs from T.H.K. and Y.-H.K. M.C. and J.S.K. performed AFM characterizations with input from Y.M. and X.W. Y.M. performed theoretical modeling with input and discussions from W.M. J.D. J.H. and C.-W.Q. Y.M. led the experiments and wrote the manuscript with inputs from S.-H.B., W.M., J.D. and L.Y. All authors contributed to discussing and revising manuscript. S.-H.B. and L.Y. supervised the project.

Competing interests

The authors declare no competing interests.

Supplementary information

Supplementary Note 1 ~ Note 26, including Supplementary Figures S1 ~ S33 and references.

Supplementary Files

This is a list of supplementary files associated with this preprint. Click to download.

- SupplementaryInformation1202.docx